DIRECT NUMERICAL SIMULATION OF FLOW PAST ELLIPTIC CYLINDERS

by

R. Mittal and S. Balachandar

Department of Theoretical and Applied Mechanics

University of Illinois at Urbana-Champaign

ABSTRACT

Flow over elliptic cylinders can be considered prototypical of flow over a range of bluff bodies since the geometry allows one to study the effect of both thickness and angle-of-attack on the flow field. Therefore a careful study of this flow should provide valuable insight into the phenomenon of unsteady separation and the structure of bluff body wakes. With this in mind, a spectral collocation technique has been developed to simulate the full three-dimensional incompressible flow over elliptic cylinders and unlike spectral element and spectral multi domain techniques, here the flow is solved in a single domain. The equations are discretized on a body fitted elliptic cylindrical grid and properties of the metric associated with this coordinate system are used to solve the governing equations in an efficient manner. Other key issues including the inflow and outflow boundary conditions and time-discretization are discussed in detail with the hope that this will facilitate future simulations of similar flows. Finally, we present results of two- and three-dimensional simulations for a range of flow and geometric parameters. The results are compared with available experimental and numerical data and it is found that the Strouhal number of the vortex shedding which is an important measure of the dynamics of the flow field, matches well with established values.

INTRODUCTION

The phenomenon of flow separation and bluff body wakes has long been intensely studied because of its fundamental significance in flow physics and its practical importance in aero and hydrodynamic applications. Flow behind a circular cylinder has become the canonical problem for studying such external separated flows[1-3]. Engineering applications on the other hand often involve flows over complex bodies like wings, submarines, missiles and rotor blades, which can hardly be modelled as a flow over a circular cylinder. Parameters such as thickness ratio and angle-of-attack, can greatly influence the nature of separation in such flows. Therefore, a richer separation phenomenon ranging from steady to unsteady and two-dimensional (2-D) to three-dimensional (3-D) is exhibited in flows over complex bodies. A fundamental study of flow over a complex non-canonical object would therefore significantly augment our current understanding of the separation process.

There are however practical reasons why separating flows over complex shapes do not lend themselves to analytical, experimental or numerical treatment so easily. Due to the complicated nature of the flow, theoretical analysis is typically limited to either flows at very low Reynolds number[4] or flows at early times after an impulsive start[5,6]. Experimental techniques have become very sophisticated in recent years but an extensive spatial and temporal analysis of the 3-D flow field would quickly overwhelm the available resources.

Numerical simulations provide a promising approach to analyzing this problem. However, a thorough analysis of such flows would require a systematic sweep of the parameter space including Reynolds number, angle-of-attack and thickness ratios and for each run, a wide range of variables would have to be measured with sufficient accuracy in both space and time, especially if turbulent structures are to be resolved adequately. The challenge for the computational fluid dynamicist would then be to first have an intelligent grid generation algorithm, second, to have an efficient solver capable of simulating the flow in the full parameter space and finally to be able to analyze and interpret the gigabytes of data that would be generated from these runs.

A systematic approach would be to start by studying a configuration which is more general than a circular cylinder and provides a richer flow behavior characteristic of typical engineering flow configurations without overburdening computational resources. Elliptic cylinders seem to provide just such a configuration and changes in cylinder eccentricity allow for shapes ranging from that of a circular cylinder to a flat plate.

There have been a few numerical simulations of flows over elliptic cylinders. Notable among these are those by Lugt and Haussling[7,8] and Blodgett[9]. Lugt and Haussling have studied the flow over thin ellipses at various angles of attack for low Reynolds numbers[7]. They have also investigated in detail the starting flow over elliptic cylinders at 45° angle-of-attack with the Reynolds number ranging between 15 and 200[8]. Blodgett[9] has performed a systematic study of 2-D flow over cylinders with various eccentricities and angles-of-attack at Reynolds number ranging up to 1000. He observes that the flow becomes increasingly complex as angle-of-attack is increased with a period doubling mechanism associated with the bifurcations. The above studies are limited to 2-D simulations and are based on the vorticity-streamfunction formulation of the Navier-Stokes equations.

In the past decade, direct numerical simulation of 3-D flows at low to moderate Reynolds number have become possible and have primarily utilized spectral methods for spatial discretization. Spectral methods provide exponential accuracy[10] through their global approximation but their application has been generally limited to simple geometries. Spectral element[11] and spectral multi-domain[12,13] methods have been developed to handle problems in complex geometries and have become quite popular in recent years. These methods provide great

flexibility in handling a broad range of geometric configuration but are computationally expensive and relatively difficult to implement.

For relatively simpler classes of geometries like elliptic cylinders, prolate/oblate spheroids and Juokowski airfoils, more specialized spectral methods based on a single domain and body fitted orthogonal grid would be expected to perform efficiently and are the method of choice. The fundamental problem with this approach is that the governing equations written in the body fitted coordinate system typically contain terms with variable coefficients which prevent a straight forward direct inversion of the discrete operators associated with the discretized equations. If methods are developed to invert these operators in an efficient manner, then the above technique can become a viable alternative to the methods indicated in the previous paragraph. A good discussion of the issues of spectral methods for complex geometries is given in a paper by Orszag[14].

This paper describes the simulation of 3-D incompressible flow over elliptic cylinders using a Fourier-Chebyshev spectral method. The accurate and efficient implementation of this methodology poses significant computational challenges. We have performed a systematic study where all the critical issues related to the spectral simulation of a complex separated flow are analyzed in detail. The purpose of this paper is twofold: novel ideas used in the simulation which are vital from the standpoint of accuracy and efficiency will be described; also, we will take this opportunity to put down our experience in terms of do's and don'ts to facilitate future simulations along similar lines. The significant features of this study can be summarized as follows:

- The governing equation are written in a body fitted elliptic cylindrical coordinate system. Special properties of the metric associated with this curvilinear coordinate system are used to develop an efficient direct solution methodology for the Helmholtz equations arising from the momentum equations and the pressure Poisson equation. This methodology can be extended to other geometries such as prolate and oblate spheroids and bipolar coordinates.
- The specification of non-reflective boundary conditions at the outflow boundary is critical especially in conjunction with direct numerical simulations[15,16]. In the present simulations, a technique similar to the buffer-domain technique of Streett & Macaraeg[13] and the viscous sponge technique of Karniadakis and Triantafyllou[1] is used to handle the specification of outflow boundary conditions. The main difference is that their techniques are implemented in conjunction with multi-domains (or multiple-elements), whereas the current methodology is based on a single domain. It is demonstrated through a specially designed numerical experiment that this boundary condition allows disturbances to convect out of the domain without any reflections.
- The body fitted coordinates used in these simulations lead to a configuration where the inflow and outflow boundaries meet at two locations. Due to the nature of the flow, prescription of a strictly Dirichlet boundary condition at the inflow section of the outer boundary and a convective boundary condition at the outflow section of the outer boundary leads to a sharp variation of flow quantities at the two junctions. To

tackle this problem, a novel mixed boundary condition is implemented at the inflow boundary which is shown to be effective in smoothing out this discontinuity.

- Time-split methods [17,18], in spite of their inherent splitting errors, are used widely in computational fluid dynamics[1,19,20]. The splitting errors originate from the approximation involved in the splitting of the operator and from the *ad-hoc* boundary conditions that are imposed at the various steps of the splitting scheme. In recent years considerable effort has gone into removing or reducing these errors[21-24]. In this paper we outline an efficient method for the removal of the errors associated with the imposition of *ad-hoc* boundary conditions for a two-step time-split scheme. This method is based on an influence matrix technique[25] and is similar in spirit to the technique used by Marcus[26]. It is also demonstrated that for the current simulations the conventional time-split method does a very satisfactory job in predicting all quantities including surface pressure, the quantity of prime engineering importance.
- A number of test cases have been run and both 2-D and 3-D results are presented. The geometrical and flow parameters are chosen to give a good representation of the full parameter space. Quantities like drag coefficients and Strouhal numbers are compared with existing experimental results in order to validate the current simulations.

SIMULATION METHODOLOGY

Coordinate System and Governing Equations

Elliptic cylindrical coordinates are made up of confocal ellipses and hyperbolas and form an orthogonal system. The mapping between Cartesian (x,y,z) and elliptic coordinates (ξ,η,z) is given by

$$x = a\cosh\xi\cos\eta\ ;\quad y = a\sinh\xi\sin\eta\ ;\quad z = z \tag{1}$$

where a is the distance between the center and the foci of the ellipse. Lines of constant ξ correspond to confocal ellipses and lines of constant η to hyperbolas. The elliptic coordinate system introduces the following metrics in the three mutually orthogonal directions

$$h_\xi = h_\eta = h = a\sqrt{sinh^2\xi + sin^2\eta}\ ,\ h_z = 1 \tag{2}$$

The governing equations of the flow are the incompressible Navier-Stokes equations which in the elliptic coordinate system take the form

$$\textit{Continuity}: \qquad \frac{1}{h^2}\left[\frac{\partial}{\partial\xi}(hu) + \frac{\partial}{\partial\eta}(hv) + h^2\frac{\partial}{\partial z}w\right] = 0 \tag{3}$$

$$\textit{Momentum conservation}: \qquad \frac{\partial \boldsymbol{u}}{\partial t} + \boldsymbol{NL(u)} = -\nabla P + \frac{1}{\mathrm{Re}}\boldsymbol{D(u)} \tag{4}$$

where (u,v,w) are the contravariant velocity components along the (ξ,η,z) directions respectively. Also $\boldsymbol{NL(u)}$ is the non-linear convective term and $\boldsymbol{D(u)}$ is the diffusion term. In elliptic coordinates these term are

$$NL(\boldsymbol{u}) = \begin{Bmatrix} \frac{u}{h}\left[\frac{\partial u}{\partial \xi} + \frac{v}{h}\frac{\partial h}{\partial \eta}\right] + \frac{v}{h}\left[\frac{\partial u}{\partial \eta} - \frac{v}{h}\frac{\partial h}{\partial \xi}\right] + w\frac{\partial u}{\partial z} \\ \frac{u}{h}\left[\frac{\partial v}{\partial \xi} - \frac{u}{h}\frac{\partial h}{\partial \eta}\right] + \frac{v}{h}\left[\frac{\partial v}{\partial \eta} + \frac{v}{h}\frac{\partial h}{\partial \xi}\right] + w\frac{\partial v}{\partial z} \\ \frac{u}{h}\frac{\partial w}{\partial \xi} + \frac{v}{h}\frac{\partial w}{\partial \eta} + w\frac{\partial w}{\partial z} \end{Bmatrix} \tag{5}$$

$$D(\boldsymbol{u}) = \begin{Bmatrix} \frac{1}{h^2}\left[\frac{\partial^2 u}{\partial \xi^2} + \frac{\partial^2 u}{\partial \eta^2}\right] + \frac{\partial^2 u}{\partial z^2} - \frac{u}{h^3}\left[\frac{\partial^2 h}{\partial \xi^2} + \frac{\partial^2 h}{\partial \eta^2}\right] + \frac{2}{h^3}\left[\frac{\partial v}{\partial \xi}\frac{\partial h}{\partial \eta} - \frac{\partial v}{\partial \eta}\frac{\partial h}{\partial \xi}\right] \\ \frac{1}{h^2}\left[\frac{\partial^2 v}{\partial \xi^2} + \frac{\partial^2 v}{\partial \eta^2}\right] + \frac{\partial^2 v}{\partial z^2} - \frac{v}{h^3}\left[\frac{\partial^2 h}{\partial \xi^2} + \frac{\partial^2 h}{\partial \eta^2}\right] - \frac{2}{h^3}\left[\frac{\partial u}{\partial \xi}\frac{\partial h}{\partial \eta} - \frac{\partial u}{\partial \eta}\frac{\partial h}{\partial \xi}\right] \\ \frac{1}{h^2}\left[\frac{\partial^2 u}{\partial \xi^2} + \frac{\partial^2 u}{\partial \eta^2}\right] + \frac{\partial^2 u}{\partial z^2} \end{Bmatrix} \tag{6}$$

Note that extra terms and variable coefficients are introduced due to the metric and curvilinear nature of the coordinate system. The above equations have been non-dimensionalized using the semi-major axis (L_x) of the ellipse as the length scale and the freestream velocity (U_∞) as the velocity scale. The Reynolds number is thus given by $\mathrm{Re} = L_x U_\infty / \nu$ where ν is the kinematic viscosity. The other important parameters are the three dimensionless geometric quantities: thickness ratio ($\mathcal{T}$), angle-of-attack (α) and spanwise aspect ratio (A). The thickness ratio of the ellipse is given by $\mathcal{T} = L_y/L_x$, where L_y is the length of the semi-minor axis, and the spanwise aspect ratio $A = L_z/L_x$ where L_z is the length of the elliptic cylinder in the z direction.

Spatial Discretization

A Fourier-Chebyshev collocation scheme is used for the spatial discretization of the governing equations. A Chebyshev expansion is used in the wall normal (ξ) direction and the Gauss-Lobatto collocation points are computed as

$$\xi_i = \frac{1}{2}\cos\left[\frac{\pi(i-1)}{(N_\xi - 1)}\right](\xi_E - \xi_O) + \frac{1}{2}(\xi_E + \xi_O) \quad \text{For} \quad i = 1, 2 \ldots, N_\xi \tag{7}$$

where ξ_E represents the elliptic cylinder, ξ_O represents the imaginary ellipse which forms the outer limit of the computational domain and N_ξ the number of grid points in the wall normal direction. ξ_E and ξ_O can be computed in terms of the other geometric parameters as $\xi_E = \frac{1}{2}\ln\left[\frac{1+\mathcal{T}}{1-\mathcal{T}}\right]$ and $\xi_O = \ln\left[x_O \cosh\xi_E + \sqrt{x_O^2 \cosh^2\xi_E - 1}\right]$ where x_O is the distance of the imaginary outer ellipse

measured along the abscissa. Also, the distance between the center and the foci of the ellipse is given by $a = (\cosh \xi_E)^{-1}$.

The circumferential direction (η) is intrinsically periodic with period 2π and a Fourier expansion is employed along this direction. The collocation points along this direction are thus computed as $\eta_j = 2\pi(j-1)/N_\eta$ for $j=1,2,.....,N_\eta$ where N_η is the number of grid points in this direction. Also the elliptic cylinder is considered to be of infinite length in the spanwise (z) direction. Thus, as long as the actual length is taken to be longer than the spanwise correlation length, this direction too can be assumed to be periodic and a Fourier expansion can be used. The correlation length can be dependent on factors like Reynolds number and angle-of-attack and thus the value of L_z chosen may be different for different simulations. The collocation points along this direction are uniformly distributed and are given by $z_k = A(k-1)/N_z$ for $k=1,2,.....,N_z$ where N_z is the number of grid points in the spanwise direction. A representative 2-D grid is shown in figure (1).

Temporal Discretization

A time-split method has been used to advance the solution in time. This method relies on the idea of operator splitting to uncouple the pressure computation from that of the velocity field and provides an efficient method for solving the incompressible Navier-Stokes equations. The theory for this method is quite well developed[17,18] and it has been successfully used in a variety of flow configurations[1,19,20]. The typical two-step version of the time-split method advances the solution from time level 'n' to '$n+1$' through an intermediate level. In the present simulations, the first step is the advection-diffusion step and it proceeds as follows:

$$\frac{\boldsymbol{u}^* - \boldsymbol{u}^n}{\Delta t} + \boldsymbol{NL}(\boldsymbol{u}) = \frac{1}{\mathrm{Re}}\boldsymbol{D}(\boldsymbol{u}) \quad in \ \Omega \tag{8}$$

$$\boldsymbol{u}^* = \boldsymbol{u}_E \quad on \ \partial\Omega_E \tag{9}$$

$$\boldsymbol{B}(\boldsymbol{u}^*) = 0 \quad on \ \partial\Omega_O \tag{10}$$

where Ω refers to the interior of the computational domain and $\partial\Omega_E$ and $\partial\Omega_O$ refer to the cylinder surface and outer boundary respectively. Details of the boundary conditions (9) and (10) will be given in a later section. The advection-diffusion step is followed by the pressure correction step

$$\frac{\boldsymbol{u}^{n+1} - \boldsymbol{u}^*}{\Delta t} = -\nabla P^{n+1} \quad in \ \Omega \tag{11}$$

$$\nabla \cdot \boldsymbol{u}^{n+1} = 0 \quad in \ \Omega \tag{12}$$

$$\boldsymbol{u}^{n+1} \cdot \tilde{\tau}_\xi = \boldsymbol{u}^* \cdot \tilde{\tau}_\xi \quad on \ \partial\Omega \tag{13}$$

where $\partial\Omega = \partial\Omega_E + \partial\Omega_O$ and $\tilde{\tau}_\xi$ is the unit vector tangent to the ξ direction. Note that the pressure correction step is in itself a set of inviscid equations and is thus well posed only if the boundary condition on the normal velocity component is imposed. Eqns. (11) and (12) together give a Poisson equation for pressure which is solved and the pressure correction is added to the intermediate

velocity u^* viz.:

$$\nabla^2 P^{n+1} = \frac{\nabla . u^*}{\Delta t} \quad in \ \Omega \tag{14}$$

$$u^{n+1} = u^* - \Delta t \nabla P^{n+1} \quad in \ \Omega + \partial\Omega \tag{15}$$

Thus the pressure step is viewed as the projection of the velocity field into the divergence free space.

To avoid severe viscous stability limits, all the terms in the wall-normal (ξ) diffusion term except the cross terms are treated implicitly using a Crank-Nicolson scheme. All non-linear advection terms, wall-tangential (η and z) viscous terms and the cross-terms in the wall-normal diffusion term are treated explicitly using a third order Adams-Bashforth scheme. This scheme is chosen in order to ensure stability in the limiting case of pure advection.

Boundary Conditions

Application of appropriate and well posed boundary conditions at the cylinder and at the outer boundary is crucial for the present simulations. Appropriate inflow and outflow boundary conditions are applied on different sections of the computational boundary as shown in figure (2). Details of the various boundary conditions are given in the following sections.

Inflow Boundary Condition

The most straightforward inflow boundary condition is the Dirichlet boundary condition specifying the inflow as the potential flow. This follows from the reasonable assumption that far upstream of the body, the displacement effect of the body is negligible and thus the flow is very close to potential flow. This inflow boundary condition has been used in almost all simulations of flow over bodies varying in shape from streamlined to bluff. In reality, the behavior at the outer boundary becomes clear if one considers the perturbation velocity (where 'perturbation' refers to the perturbation from potential flow). The momentum defect in the wake appears as an inflow in the perturbation velocity which is balanced by an outflow over the rest of the outer boundary. This perturbation outflow is maximum in the region directly above and below the body and reduces in the upstream region. Furthermore, the flow encounters a body which is more bluff than the actual shape due to the displacement effect and thus, the flow tends to accelerate more than potential flow as it goes over the body. By imposing the potential flow as the Dirichlet boundary condition at the inflow, the displacement effects are not allowed at the inflow part of the outer boundary whereas at the outflow part, where a convective boundary condition is imposed, the flow is able to adjust to the presence of the body. This leads to a sharp variation of velocity at the junction of the inflow and outflow sections of the outer boundaries. This discontinuity, though fairly small in magnitude compared to the potential velocity, is enough to generate oscillations associated with the Gibbs phenomenon and its effect is felt in the whole domain due to the global nature of the computations.

It should be pointed out that there are advantages to using a computational grid (and domain) based on the natural coordinates. Such grids are simple to construct and no complicated grid generation routines are required. Furthermore, the same grid and domain can be used to study flows at different angles-of-attacks. However, such a computational domain makes the simulations more sensitive to the boundary conditions at the outer boundary. In conventional simulations with a box like computational domain, the inflow and outflow segments are clearly separated by a change in the coordinate, thereby isolating any discontinuity at the corner points. The same is not true for the computational domain used in the present simulations and extra care needs to be taken to ensure that boundary conditions applied at the outer boundary are compatible with the nature of the flow field and lead to a well behaved solution.

Thus, there is a need to devise an inflow boundary condition which will smooth out the discontinuity in the vicinity of the inflow-outflow junction. The boundary condition should be based on the physics of the flow and provide a way for the flow to react to the blockage effect of the cylinder. Also we require Dirichlet boundary condition over most of the inflow boundary so as to maintain control on the incoming flow. Keeping this in mind, the following mixed boundary condition is used at the inflow boundary

$$B(\boldsymbol{u}^*) \;=\; \boldsymbol{u} - \boldsymbol{u}_{in} + [1 - f(\xi_O,\eta)]\left(\frac{\partial \boldsymbol{u}}{\partial \xi} - \frac{\partial \boldsymbol{u}_{pot}}{\partial \xi}\right) \;=\; 0 \quad on \;\; \partial\Omega_{in} \tag{16}$$

where $\partial\Omega_{in}$ is the inflow part of the outer boundary. $f(\xi_O,\eta)$ is a filter function on the outer boundary and will be defined in the next section. For the present discussion it suffices to say that this filter function varies smoothly from a value of one in the upstream region to a value slightly less than one at the inflow-outflow junction. Thus, since the coefficient of the Neumann term is small, the above boundary condition is primarily a Dirichlet boundary condition. The small Neumann part is however very crucial in that it allows the flow some freedom in the vicinity of the inflow-outflow junction. The boundary condition smoothly goes to a purely Dirichlet condition in the front portion of the inflow boundary. $\boldsymbol{u}_{in}$ is the Dirichlet part of the inflow boundary condition and is specified as

$$\boldsymbol{u}_{in} \cdot \tilde{\tau}_{\xi} = \boldsymbol{u}_{pot} \cdot \tilde{\tau}_{\xi} \;\; ; \;\; \boldsymbol{u}_{in} \cdot \tilde{\tau}_{\eta \text{ or } z} \;=\; \left\{\boldsymbol{u}_{pot} \;+\; \Delta t(2\nabla P^n - \nabla P^{n-1})\right\} \cdot \tilde{\tau}_{\eta \text{ or } z} \tag{17}$$

Due to the slip velocity (here 'slip' refers to the deviation from the potential velocity) which results at the end of the pressure correction step in the time-split formulation, the tangential velocity component of the inflow can not be enforced exactly . The above formula has been suggested by Street & Hussaini[27] in order to reduce the slip error to $O(\Delta t^3)$. Thus, the above specification ensures that in the strictly Dirichlet portion of the inflow boundary, the normal velocity is exactly equal to the potential value and the tangential components are equal to the corresponding potential values up to $O(\Delta t^3)$. The mixed boundary condition is based on the overall reasoning that far upstream of the body, the perturbation from the potential flow is very small. It should be pointed out that a number of other boundary conditions (combination of Dirichlet with second derivative for

instance) could be used which would also allow for a similar behavior but since the above boundary condition works well in our simulations, we have not tested other boundary conditions.

In figure (3) we provide evidence of the beneficial effect of using the mixed boundary condition on the inflow boundary. The result shown is for a simulation with $\mathcal{T}$=0.5, α=0° and Re=1000. In figure (3a) we compare $u'(= u - u_{pot})$ at the outer boundary obtained with the two different inflow boundary conditions. Figure (3b) shows the corresponding v' values. Both figures show that the simulation using Dirichlet boundary conditions suffers from the Gibbs phenomenon whereas the mixed boundary condition shows negligible spurious oscillations. It should be noted that this is at an early stage in the simulation (t=2.5) and the values of the perturbation are themselves small. However, the fact that the Gibbs phenomenon is apparent so early shows just how much damage a badly posed boundary condition can do. With the mixed boundary condition, the displacement effect due to the body is allowed to propagate upstream thereby adjusting the flow and resulting in a well behaved solution.

Outflow Boundary Condition

Specification of outflow boundary condition has long been an outstanding issue in the computation of incompressible external flows. A number of techniques have been proposed for solving problems in semi-infinite domains. The first one is to expand along the semi-infinite direction in terms of Laguerre polynomials. This method to our knowledge, has not been investigated in any detail. The second technique proposed for external flow simulations is to use a coordinate stretching and map the infinite or semi-infinite domain to a finite one and then to specify the far-field boundary conditions at the outer boundary. The choice of the stretching function is very critical[28,29] when using spectral methods and it is still not clear how well such a methodology would work in the case of highly unsteady and turbulent bluff body wakes.

The third technique is that of domain truncation where the semi-infinite domain is truncated to a large but finite domain and the simulation is carried out in this truncated domain. The critical aspect of implementing this technique is the boundary condition at the outflow boundary. In the context of finite-difference simulations of a compressible flow over circular cylinders, simple outflow boundary conditions based on primitive variables have been shown to result in spurious secondary frequencies[16]. Such boundary conditions are catastrophic in spectral simulations due to their extreme sensitivity and only carefully derived characteristic variable boundary conditions produce stable and consistent results[15,16].

For spectral simulations of incompressible flows, non-reflective boundary conditions have been proposed and successfully employed in conjunction with domain truncation. Notable among these are the buffer-domain[13] and viscous-sponge[1] techniques. These techniques recognize the fact that the source of possible reflections from the outflow boundary is in the elliptic nature of the governing equation arising from the viscous terms and the pressure field. The idea is to effectively

remove this ellipticity at the outflow boundary. Here we have implemented this technique on a single domain where the first source of ellipticity is removed by carefully identifying the normal (ξ) diffusion terms in the momentum equations and smoothly attenuating them to zero at the outer boundary. Similarly, the ability of the pressure field to carry signals back into the domain from the outer boundary is nullified by attenuating the source term in the pressure Poisson equation near the outflow boundary.

The attenuation of the normal diffusion and pressure source terms is carried out by multiplying the requisite terms by a filter function of the form

$$f(\xi,\eta) = 1 - \exp\left[-\gamma\left([\bar{x}(\xi)]^{\beta_1} + [\bar{\eta}(\eta)]^{\beta_2}\right)\right] \tag{18}$$

$$\bar{x}(\xi) = \frac{\cosh\xi - \cosh\xi_O}{\cosh\xi_E - \cosh\xi_O} \quad \text{and} \quad \bar{\eta}(\eta) = \frac{\eta - \eta_a}{\pi} - \varsigma \sin(2\pi\frac{\eta - \eta_a}{\pi}) \tag{19}$$

where $\xi_E \le \xi \le \xi_O$ and $\eta_a \le \eta \le \eta_a + \pi$, η_a being the η location which lies along the angle-of-attack line. The above function is reflected about the line of angle-of-attack to get its representation in the other half of the domain, ie. $\eta_a + \pi \le \eta \le \eta_a + 2\pi$. We choose to define the region where $f < 0.99$ as the filtered region (see figure (2)) where the attenuation of the normal viscous and the pressure source terms is significant. The rest of the region (where $f \ge 0.99$) will be referred to as the unfiltered region. Of course this definition is arbitrary and made only for the purpose of simplifying the following discussion. It should be stressed that there is no discontinuity in the filter at $f = 0.99$ and it varies smoothly and continuously in the whole domain. The shape and smoothness of the filter function and the extent of the filtered region can be controlled through the parameters γ, β_1, β_2 and ς. Based on our experience in applying the filter, we recommend the following general criteria in tailoring the filter function:

- The function should be smooth ie. its spectra (both Chebyshev and Fourier) should show adequate decay. $\partial f/\partial\xi$ should numerically evaluate to zero close to the body in order to avoid spurious generation of vorticity. It has been observed that any unsmoothness in ξ appears as a large first derivative near the cylinder. Instead of (18) we have attempted to use piecewise continuous filter functions of the form

$$f(\xi) = \begin{cases} 1 & \xi_E \le \xi \le \xi_f \\ e^{-\gamma\left(\frac{\xi-\xi_f}{\xi_O-\xi_f}\right)^{\beta}} & \xi_f \le \xi \le \xi_O \end{cases} \tag{20}$$

  where ξ_f is the starting location of the filtered region. Note that η dependance has been omitted here for the sake of discussion. This dependance can be built in through similar piecewise continuous η functions. This type of function gives very good control over the shape and extent of the filtered region and thus at first glance seems a good choice. Furthermore this function is analytically continuous over the entire domain and appears smooth to at least plotting accuracy. However, when the first derivative of this function is computed numerically, it shows large non-zero values

in the unfiltered region. This can lead to generation of spurious vorticity near the body, a situation which should be avoided at all costs. The problem lies in the fact that at ξ_f, the function is continuous only up to a finite order of derivatives, the order itself being equal to $\lceil \beta\text{-}1 \rceil$. Thus, such piecewise defined functions which work well in conjunction with multi-domain computations[13], are definitely not compatible with the present single-domain based simulations.

- There is one other physical requirement which is also related to the smoothness of the function in ξ. The filter region should extend over at least three wavelengths of spatial variation of the physical quantities. Joslin et al.[30] have found empirically that this length is required so that the disturbances smoothly pass through the filter region without any reflections. For the present simulations we have found that a length of 15 to 20 units is adequate for this purpose.

- Filtering should be limited to the outflow region and f should be equal to one (ie. no filtering should be applied) in the inflow region of the outer boundary. The region upstream of the cylinder "feels" and adjusts to the presence of the cylinder only though the action of diffusion and pressure. Filtering the normal viscous and pressure source terms reduces the ability of the upstream flow to adjust itself to the displacement effect of the cylinder and leads to the development of a spurious boundary layer on the inflow region of the outer boundary.

- In order to avoid any reflections and guarantee hyperbolicity of the governing equations in the ξ-direction, the normal diffusion and pressure source terms should be filtered out completely (ie. $f=0$) in the wake region of the outer boundary. It is of prime importance that all sources of ellipticity be removed effectively in this region. For simulations in curvilinear coordinates, care should be taken to carefully identify and filter all the terms which make up the normal diffusion term.

For the current simulations, the above criteria are adequately satisfied by choosing the following parameter values: $\gamma = 40$, $\beta_1 = 3.23$, $\beta_2 = 3.8$ and $\zeta = 0.15$. The advection-diffusion equation is thus explicitly parabolized (or hyperbolized in direction normal to the boundary) in the wake region at the outer boundary. Outside the wake region, the diffusive effects are negligible and the flow is basically convective in nature. Thus, flow at the entire outflow boundary can be treated as being purely convective in the direction normal to the boundary and convective boundary conditions can be employed without generating any kind of a spurious boundary layer. Finally, the exact form of the advection diffusion equation (Eq. (8)) is

$$f(\xi,\eta)\frac{\partial^2 \boldsymbol{u}^*}{\partial \xi^2} + \boldsymbol{F}(\xi,\eta)\boldsymbol{u}^* - \frac{2\,\mathrm{Re}}{\Delta t}h^2\boldsymbol{u}^* = \boldsymbol{RHS} \quad in\ \Omega \tag{21}$$

where the first two terms on the LHS are the normal diffusion terms that are treated implicitly ($\boldsymbol{F}(\xi,\eta)$ being the variable coefficient of the $\boldsymbol{u}^*$ term) and $\boldsymbol{RHS}$ consists of all the terms treated explicitly. In the wake region of the outer boundary, the above equation is primarily convective, since $f = 0$ in that region. The convective boundary condition in (10) is then given by

$$B(u^*) = u^* - \frac{RHS}{\left[F(\xi,\eta) - \frac{2\mathrm{Re}}{\Delta t}h^2\right]} = 0 \quad on \ \partial\Omega_{out} \tag{22}$$

where $\partial\Omega_{out}$ is the outflow portion of the outer boundary.

Furthermore, after incorporating the filter function, the final form of the pressure Poisson equation is given by

$$\frac{1}{h^2}\left\{\frac{\partial^2 P^{n+1}}{\partial\xi^2} + \frac{\partial^2 P^{n+1}}{\partial\xi^2}\right\} + \frac{\partial^2 P^{n+1}}{\partial z^2} = f(\xi,\eta)\frac{\nabla . u^*}{\Delta t} \quad in \ \Omega \tag{23}$$

(13) and (15) together give the following boundary condition for pressure

$$\nabla P^{n+1} . \tilde{\tau}_\xi = 0 \quad on \ \partial\Omega_O \tag{24}$$

which is enforced over the entire outer boundary. It should be noted that alteration of the pressure Poisson equation leads to non-zero divergences in the filter region and thus amounts to introducing artificial compressibility there. Also, with the viscous filter, the momentum equation can be viewed as a variable viscosity problem and therefore, applying the divergence-free condition on the momentum equation will not lead to a typical Pressure Poisson equation. The time-split method then becomes the most straightforward way of decoupling pressure from the momentum equation.

It should be added here that for a small computational domain it might be better to formulate the Poisson equation in terms of the perturbation pressure[31] thereby requiring the pressure to approach the potential pressure instead of zero at the outflow boundary. For our computations we find that doing so does not make any significant difference in the solution. Furthermore, Street & Macaraeg[13] find it useful to linearize the convection term about the potential flow in the buffer domain. This helps to ensure that the convection at the outflow boundary is strictly in the outgoing direction. However, convecting disturbances out of the computational domain at the potential velocity instead of the actual velocity results in increased mass imbalance between net inflow and outflow. For the present simulation, the outflow boundary is sufficiently downstream of the body and it is very unlikely that even in the wake, the flow at the outflow boundary will ever reverse direction. Therefore, we choose not to linearize the convection term, however, we do check to make sure that the condition of strict outflow on the outflow boundary is never violated.

Boundary Conditions on the Body

Since the advection-diffusion step is a viscous step, the obvious choice for the boundary condition (9) at the solid body is no-slip and no-penetration ie. $u_E = 0$. In order to guarantee no penetration at the end of the full time step, the boundary condition for pressure on the surface of the elliptic cylinder is given by the Neumann boundary condition

$$\nabla P^{n+1} . \tilde{\tau}_\xi = 0 \quad on \ \partial\Omega_E \tag{25}$$

where $\partial\Omega_E$ refers to the body surface. However, since the tangential gradients of pressure on the cylinder are not specified, this combination of boundary conditions results in a finite slip velocity of $O(\Delta t)$ on the cylinder surface. Using the same idea that was used in (17), the slip error can be reduced to $O(\Delta t^3)$ by providing a boundary condition for the intermediate tangential velocity component, which will partially nullify the tangential pressure gradient[27]. This improved higher order boundary condition is given by

$$\boldsymbol{u}_E \cdot \tilde{\tau}_{\eta \text{ or } z} = \Delta t(2\nabla P^n - \nabla P^{n-1}) \cdot \tilde{\tau}_{\eta \text{ or } z} \quad on \ \partial\Omega_E \tag{26}$$

Orszag et al.[21] and Karniadakis et al.[22] have systematically analyzed the splitting errors and the resulting numerical boundary layer that develops close to the no-slip boundary. They have suggested higher-order extrapolation methods and improved pressure and intermediate velocity boundary conditions to reduce these errors[21-23]. Perot[24] has provided an alternative approach for analyzing the splitting errors where he views the split method as an approximate block LU decomposition of the fully coupled system of equations. He then presents generalized block LU decompositions which allow for arbitrary higher order accuracy.

The time-split method with the above boundary conditions (eqns.(25) and (26)) has been used in the past to simulate a number of different types of flows including Taylor-Couette flow[27] and turbulent square duct flow[32] and has lead to satisfactory results. However, in the present simulations, Eq. (25) may be a poor approximation especially at front stagnation, separation and reattachment points. Also in separated flows, the initial roll up and vortex shedding process may be influenced by the non-zero slip velocity on the body. To test the performance of the above boundary conditions it was decided to have an alternate formulation of the time-split scheme where both the no-slip and the correct pressure boundary condition would be satisfied exactly. Following Marcus[26], an influence-matrix technique has been implemented in conjunction with the time-split method. This implementation differs from the Kleiser and Schumann[25] influence-matrix technique which avoids all time-split errors. The use of the viscous filter makes the implementation of the Kleiser-Schumann's complete influence-matrix method difficult.

The current implementation of the influence-matrix technique which is done in conjunction with the time-step scheme, basically adjusts the intermediate wall-normal and tangential velocity components such that at the end of the pressure correction step, no-slip and no-penetration conditions are satisfied exactly and the pressure satisfies the wall-normal momentum equation as follows:

$$\boldsymbol{u}^{n+1} = 0 \quad \text{and} \quad \nabla P^{n+1} \cdot \tilde{\tau}_\xi = \frac{1}{\mathrm{Re}} \nabla^2 \boldsymbol{u}^{n+1} \cdot \tilde{\tau}_\xi \quad on \ \partial\Omega_E \tag{27}$$

Thus the boundary conditions are consistent with those of the full Navier-Stokes equations. Marcus[26] has used an influence-matrix technique in conjunction with a three-step time-split scheme whereas in the current simulations we implement it with a two-step scheme. There are subtle

differences between the two as far as the specification of (27) is concerned. Details of the formulation of this technique are given in the appendix. The results obtained from the time-split scheme with and without the influence matrix method will be discussed in the results section.

Initial Conditions

Potential flow is specified as the initial condition for the flow computation. Thus, the initial flow field is divergence free, a necessary condition for well posedness of the equations. For the non-zero angle-of-attack case, no artificial perturbation is needed to initiate vortex shedding and by specifying the initial condition as potential flow, conditions for the real startup process are simulated accurately. For the case of zero angle-of-attack, an artificial perturbation needs to be given to the flow in order to break the symmetry about the x-axis and initiate the shedding process. In addition to this, for 3-D simulations, a perturbation also needs to be given along the spanwise direction in order for the flow to develop three-dimensionality.

Two desirable properties of any artificial perturbation are that it should neither introduce any divergence nor any net circulation. Also from a practical point of view, the perturbation should achieve its goal (induce shedding or three-dimensionality) in the shortest possible time. For breaking the symmetry about the x axis, we impose a slip velocity on the surface of the cylinder sinusoidally (a conveyor-belt type mechanism) for a short period of time. An alternative would be to vary the angle of the incoming flow at the outer boundary but it takes longer for the shedding to start from this type of perturbation than when the conveyor-belt type mechanism is used. Perturbations given at the inflow have to convect downstream before they reach the cylinder and thus the full effect of the perturbation is felt only after a time which is roughly equal to x_O. This is not the case for the conveyor-belt type mechanism since the perturbation is given on the cylinder surface itself. For the spanwise perturbations, a small random spanwise variation is given to the slip velocity at the cylinder for a short period of time and the three-dimensional flow is allowed to develop on its own subsequently.

Solution Algorithm

The overall solution procedure consists of two steps. The first step is the advection-diffusion step, where the discretized version of Eq. (21) is solved to obtain the intermediate velocity $\boldsymbol{u}^*$. Due to the explicit discretization of the advection-diffusion equation along the η and z directions, Eq. (21) is simply a set of uncoupled ordinary differential equations in ξ for various η and z locations. Since at any given η location, $\boldsymbol{F}$ is a function of ξ only, Eq. (21) is a set of variable coefficient 1-D Helmholtz equations which can be solved easily by computing the inverse of the discretized operator. Since the operator is independent of z, there are only as many operators as there are η points and thus storage of their inverses is not memory intensive.

To satisfy incompressibility exactly at the end of each time-step, the pressure Poisson equation must be solved in a fully implicit manner. Therefore, efficient solution of the three dimensional

pressure Poisson equation is the key issue. One approach is to use iterative schemes such as preconditioned conjugate gradient or multigrid methods. The other approach is the direct method where the operator is inverted without resorting to iterative schemes. Here we have developed an efficient direct solver for the 3-D Poisson equation in elliptic cylindrical coordinates. The orthogonal curvilinear elliptic cylindrical coordinate system introduces a non-separable variable coefficient into the Poisson equations as shown below

$$\frac{1}{a^2(\sinh^2\xi + \sin^2\eta)}\left\{\frac{\partial^2 P}{\partial\xi^2} + \frac{\partial^2 P}{\partial\eta^2}\right\} + \frac{\partial^2 P}{\partial z^2} = G'(\xi,\eta,z) \tag{28}$$

where $G'(\xi,\eta,z)$ represents the source term of the pressure Poisson equation (Eq. (23)). In the context of a spectral simulation, the dependence of this coefficient on the circumferential coordinate (η) hinders straightforward Fourier transform along this direction. Multiplying out by h^2, the above equation is rewritten as

$$\frac{\partial^2 P}{\partial\xi^2} + \frac{\partial^2 P}{\partial\eta^2} + a^2(\sinh^2\xi + \sin^2\eta)\frac{\partial^2 P}{\partial z^2} = G(\xi,\eta,z) \tag{29}$$

where $G(\xi,\eta,z)$ is the source term multiplied by h^2. Now it can be seen that the variable coefficient in the above equation has a limited bandwidth when transformed in the circumferential direction and this property is exploited in developing the direct solution algorithm. First the equation is Fourier transformed in the z direction in a straightforward manner. The next step is to transform the equation in the η direction and this requires transforming the quantity $\sin^2\eta\hat{P}(\xi,\eta,k_z)$ where the 'hat' refers to z-transformed values and k_z represents wavenumber along the z-direction. Using the definition

$$\sin^2\eta = \frac{1}{2} - \frac{e^{2i\eta}}{4} - \frac{e^{-2i\eta}}{4} \tag{30}$$

the Fourier coefficients of $\sin^2\eta\hat{P}(\xi,\eta,k_z)$ can be written in terms of the Fourier coefficients of $\hat{P}$ as

$$\widehat{\sin^2\eta\hat{P}}|_{k_\eta} = \frac{\hat{\hat{P}}}{2}|_{k_\eta} - \frac{\hat{\hat{P}}}{4}|_{k_{\eta-2}} - \frac{\hat{\hat{P}}}{4}|_{k_{\eta+2}} \tag{31}$$

where double hat now refers to quantities transformed in both z and η directions. Here k_η represents wavenumber in the η direction. Thus, the transformed equation for the (k_η, k_z) mode becomes

$$\frac{\partial^2\hat{\hat{P}}|_{k_\eta}}{\partial\xi^2} - \left[k_\eta^2 + a^2(\sinh^2\xi + \frac{1}{2})k_z^2\right]\hat{\hat{P}}|_{k_\eta} + a^2k_z^2\hat{\hat{P}}|_{k_{\eta-2}} + a^2k_z^2\hat{\hat{P}}|_{k_{\eta+2}} = \hat{\hat{G}}|_{k_\eta} \tag{32}$$

where the dependence of $\hat{\hat{P}}$ and $\hat{\hat{G}}$ on k_z is not explicitly shown. The above system of equations is uncoupled for the Fourier modes in the z direction ($k_z = 0, \pm 2\pi/A, \pm 4\pi/A, \ldots\ldots, \pm N_z\pi/A$) and each mode can be considered independently. Moreover, the odd and even modes in η are decoupled and two separate problems, one for the odd modes

$(k_\eta = -\frac{N_\eta}{2}+1, -\frac{N_\eta}{2}+3, \ldots\ldots, \frac{N_\eta}{2}-1)$ and one for the even $(k_\eta = -\frac{N_\eta}{2}+2, -\frac{N_\eta}{2}+4, \ldots\ldots, \frac{N_\eta}{2})$ can be solved separately. Let k_{o_j} denote the j^{th} odd η mode and k_{e_j} the j^{th} even η mode. The subsequent discussion will be limited to the solution of the odd modes; the corresponding procedure for the even modes can be obtained simply by changing k_o to k_e. Now when the Chebyshev collocation along ξ is also incorporated, for each k_z mode, the fully discretized version of Eq. (32) for the odd η modes becomes

$$\left[[D_{c2}] - k_{o_j}^2[I] - [E]\right]\hat{\hat{P}}|_{k_{o_j}} + a^2k_z^2[I]\hat{\hat{P}}|_{k_{o_{j-1}}} + a^2k_z^2[I]\hat{\hat{P}}|_{k_{o_{j+1}}} = \hat{\hat{G}}|_{k_{o_j}} \tag{33}$$

where $[D_{c2}]$ is the Chebyshev collocation second derivative matrix, $[I]$ is the identity matrix and $\hat{\hat{P}}$ and $\hat{\hat{G}}$ are vectors which contains the values of $\hat{\hat{P}}$ and $\hat{\hat{G}}$ at the N_ξ collocation points respectively. Furthermore, the diagonal matrix $[E]$ is given by

$$[E]_{il} = \begin{cases} a^2(\sinh^2\xi_i + \frac{1}{2})k_z^2 & \text{if } i = l \\ 0 & otherwise \end{cases} \tag{34}$$

where ξ_i refers to the i^{th} Chebyshev collocation location given by (7). The above system of equations can be represented as a block tridiagonal system as follows:

$$\begin{bmatrix} [A_1] & [B] & & & & \\ [B] & [A_2] & [B] & & 0 & \\ & \ddots & \ddots & \ddots & & \\ & & & [B] & [A_{N_\eta/2-1}] & [B] \\ & 0 & & & [B] & [A_{N_\eta/2}] \end{bmatrix} \begin{Bmatrix} \boldsymbol{P}|_{k_{o_1}} \\ \boldsymbol{P}|_{k_{o_2}} \\ \vdots \\ \boldsymbol{P}|_{k_{o_{(N_\eta/2-1)}}} \\ \boldsymbol{P}|_{k_{o_{(N_\eta/2)}}} \end{Bmatrix} = \begin{Bmatrix} \boldsymbol{G}|_{k_{o_1}} \\ \boldsymbol{G}|_{k_{o_2}} \\ \vdots \\ \boldsymbol{G}|_{k_{o_{(N_\eta/2-1)}}} \\ \boldsymbol{G}|_{k_{o_{(N_\eta/2)}}} \end{Bmatrix} \tag{35}$$

where the double hats denoting transformed values have been removed from the above equations and from the following discussion for ease of presentation. Also, in the above equation, $[A_j] \equiv [D_{c2}] - k_{o_j}^2[I] - [E]$ and $[B] \equiv a^2k_z^2[I]$

Boundary conditions for pressure can be easily incorporated within this formulation. Periodic boundary conditions along η and z are implicitly built into the Fourier expansion along these directions. Dirichlet boundary conditions in the ξ direction can be built into the matrix representation by appropriately modifying the first and the last rows of the matrix operators and the corresponding elements of the right-hand-side vectors $\boldsymbol{G}$. Neumann boundary conditions can be incorporated by using the reduced matrix technique and modifying $[A]$ and $\boldsymbol{G}$ appropriately[33].

The block-tridiagonal equation (35) is solved by the Thomas algorithm, which consists of two steps. First is the forward substitution step in which the lower diagonal terms are zeroed out resulting

in the following block upper triangular system

$$\begin{bmatrix} [A_1^*] & [B] & & & \\ & [A_2^*] & [B] & 0 & \\ & & \ddots & \ddots & \\ & 0 & & [A^*_{N_\eta/2-1}] & [B] \\ & & & & [A^*_{N_\eta/2}] \end{bmatrix} \begin{Bmatrix} \boldsymbol{P}|_{k_{o_1}} \\ \boldsymbol{P}|_{k_{o_2}} \\ \vdots \\ \boldsymbol{P}|_{k_{o_{(N_\eta/2-1)}}} \\ \boldsymbol{P}|_{k_{o_{(N_\eta/2)}}} \end{Bmatrix} = \begin{Bmatrix} \boldsymbol{G}^*|_{k_{o_1}} \\ \boldsymbol{G}^*|_{k_{o_2}} \\ \vdots \\ \boldsymbol{G}^*|_{k_{o_{(N_\eta/2-1)}}} \\ \boldsymbol{G}^*|_{k_{o_{(N_\eta/2)}}} \end{Bmatrix} \tag{36}$$

where the $[A_j^*]$ matrices are related to the $[A_j]$ matrices in the following way

$$[A_j^*] = [A_j] - [B]\ [A^*_{j-1}]^{-1}\ [B] \qquad \text{for } j = 2, 3, ..., N_\eta/2 \tag{37}$$

Correspondingly, the modified right-hand-side vectors $\boldsymbol{G}^*$ are related to the original right-hand-side vectors $\boldsymbol{G}$ by

$$\boldsymbol{G}^*|_{k_{o_j}} = \boldsymbol{G}|_{k_{o_j}} - [B]\ [A^*_{j-1}]^{-1}\ \boldsymbol{G}^*|_{k_{o_{j-1}}} \qquad \text{for } j = 2, 3, ..., N_\eta/2 \tag{38}$$

The above recursive equations for $[A^*]$ and $\boldsymbol{G}^*$ are initialized by $[A_1^*] = [A_1]$ and $\boldsymbol{G}^*|_{k_{o_1}} = \boldsymbol{G}|_{k_{o_1}}$ respectively. The forward substitution is followed by the back-substitution step and the final solution is obtained as follows

$$\boldsymbol{P}|_{k_{o_j}} = [A_j^*]^{-1} \left\{ \boldsymbol{G}^*|_{k_{o_j}} - [B]\ \boldsymbol{P}|_{k_{o_{j+1}}} \right\} \qquad \text{for } j = N_\eta/2 - 1, N_\eta/2 - 2, ..., 2, 1 \tag{39}$$

Like the forward substitution step, the back substitution is also a recursive step and recursion is initiated by $\boldsymbol{P}|_{k_{o_{(N_\eta/2)}}} = [A^*_{N_\eta/2}]^{-1}\ \boldsymbol{G}^*|_{k_{o_{(N_\eta/2)}}}$.

A naive implementation of the Thomas algorithm requires the storage of all the $[A_j^*]^{-1}$ matrices. Since these matrices are dependent on both k_η and k_z, the memory requirement for their storage is $(N_\xi^2 N_\eta N_z)$. The other option is to compute them at every time-step, but this is a computationally expensive proposition. The enormous storage or computational demands can be eased by exploiting the specific structure of $[A]$. It can be split into a dense matrix $[C]$ which depends only on k_z, and a diagonal part which depends only on k_η as follows:

$$[A_j] = [C] - k_{o_j}^2 [I] \tag{40}$$

where

$$[C] = [D_{c2}] - [E] \tag{41}$$

Now the inverse of $[A_j]$ can be conveniently written in terms of the modal matrices of $[C]$ as follows:

$$[A_j]^{-1} = [M] \left[[\lambda] - [I]\ k_{o_j}^2 \right]^{-1} [M]^{-1} \tag{42}$$

where $[M]$ is the eigenvector matrix of $[C]$, $[M]^{-1}$ is its inverse and $[\lambda]$ is the corresponding diagonal eigenvalue matrix. The inverse of $[A_j^*]$ is then given by

$$[A_j^*]^{-1} = [M]\ [\varsigma_j]\ [M]^{-1}\ for\ j = 2,3,.....,N_\eta/2 \tag{43}$$

where

$$[\varsigma_j] = \left[[\lambda] - [I]\ k_{o_j}^2 - [B][B]\ [\varsigma_{j-1}]\right]^{-1} \quad for\ j = 2,3,... ..,N_\eta/2 \tag{44}$$

The recursive relation in (44) is initialized by $[\varsigma_1] = \left[[\lambda] - [I]\ k_{o_1}^2\right]^{-1}$.

Thus the sequence of steps can be summarized as follows:

1) At the the beginning of the time-stepping, $[M]$ and $[M]^{-1}$matrices are computed and stored for each k_z. $[\lambda]$ is also computed and used to compute $[\varsigma_j]$ recursively using (44). These eigenvalues are also stored in arrays. The storage requirement is of the order of $N_\xi^2 N_z$ for the modal matrices and $N_\xi N_\eta N_z$ for $[\varsigma_j]$.

2) At every time-step

- $[A_j^*]^{-1}$is computed using (43)
- $\boldsymbol{G}^*|_{k_{o_j}}$ is computed using (38)
- $\boldsymbol{P}|_{k_{o_j}}$ is computed using (39)

Finally, two issues need to be addressed to complete the description of the solution algorithm. The first is regarding the error incurred in the computation of three outermost η modes, namely, $k_\eta = -\frac{N_\eta}{2}+1, \frac{N_\eta}{2}-1, \frac{N_\eta}{2}$. These modes are coupled to modes which are outside the computed range and are thus not computed correctly. Therefore, if these modes are not decoupled from their neighboring internal modes, the error spreads into the other computed modes and contaminates the whole solution. This decoupling can be achieved simply by zeroing out the off-diagonal block in the rows corresponding to these modes in the matrix shown in Eq. (35). Furthermore, the solution corresponding to these modes can be annulled by zeroing out the $\boldsymbol{G}^*$vector corresponding to these modes. The rest of the solution procedure follows as described previously.

The second issue concerns the non-uniqueness of the pressure Poisson equation with Neumann boundary conditions which has the consequence that pressure is evaluated only up to an additive constant. The presence of a non-unique solution is manifested through a zero eigenvalue of the $[A]$ matrix for the $k_\eta = k_z = 0$ (mean) mode. The corresponding eigenvector represents the constant mean pressure. Here in the computation of $[\varsigma_j]$ using Eq. (44), the inverse of the null eigenvalue is replaced by zero thereby effectively zeroing out the mean pressure at each time step. This procedure can be viewed as the singular value decomposition of the matrix operator.

RESULTS

2-D Simulations

Preliminary 2-D computations have been performed in order to validate the code. These computations are substantially less time and memory consuming than corresponding 3-D runs and allow us to scan the parameter space more comprehensively. In addition to this, all of the known numerical studies of flow around elliptic cylinders have been 2-D and thus a direct comparison can be made with them.

According to Joslin et al.[30] the size of the viscous filter region should be at least three wavelengths long. Also, if space correlation studies are to be performed in the wake then the unfiltered domain should contain at least 5-6 vortices. For the range of parameters that we have investigated, the above criteria are reasonably satisfied by choosing x_O in the range of 30 to 40 units. Once the size of the domain is decided, the number of grid points are chosen so that all waves travelling downstream in the wake will be resolved adequately for the parameter range studied. *A-priori* runs show that a grid with N_ξ=81 and N_η=100 for x_O=30 and N_ξ=101 and N_η=120 for x_O=40 provides adequate resolution for our simulations.

A CFL number based on the convection term in elliptic coordinates (Eq. (5)), is used as a guideline in choosing the time step. Various runs have shown that a stable time-stepping is achieved for CFL$\approx$0.1 which for the above grid corresponds to $\Delta t \approx 0.002$. These are of course typical numbers and there is some variation with Reynolds number, thickness ratio and angle-of-attack.

TEST OF THE OUTFLOW BOUNDARY CONDITION

Extensive tests have been done to study the effectiveness of the outflow boundary condition and to also determine what effect the viscous and pressure filters have on vortices travelling downstream through the filtered region to the outflow boundary. Studying vortices which are part of a Karman vortex street is not appropriate for this purpose since the presence of many vortices and of a body which is continuously producing vorticity, would make the results hard to interpret. Thus, a special simulation has been designed where a pair of vortices can be studied in isolation as they travel downstream. The simulation starts with the usual no-slip boundary conditions on the cylinder, mixed boundary condition at the inflow and non-reflective boundary conditions at the outflow boundary. These boundary conditions are maintained till the two vortices which were attached to the cylinder have grown to their full strength (which corresponds to t=12.5). At this time, the no-slip boundary condition is removed and potential velocities are imposed at the body. As a result, the two vortices detach from the cylinder and start convecting downstream. At the same time the strength of the vorticity layer on the cylinder starts to reduce and the flow begins to approach potential flow.

The parameters chosen for this study are $\mathcal{T}$=0.5, α=0° and Re=500. A smaller computational domain with x_O=20 is chosen in the interest of saving CPU time and the filtered region starts at x=10.

Since we just have a pair of vortices, a smaller computational and filter region should be adequate. The first set of results presented in figure (4) is a sequence of vorticity contour plots which show the two vortices as they convect downstream through the filtered region and out of the computational domain. A slice of the whole computational domain has been extracted for plotting purposes. Furthermore, in all the contour plots, contours corresponding to the same vorticity values have been plotted so that changes in shape of the vortices can be followed as they travel downstream.

Figure (4a) shows the vortices before they enter the filtered region. The two small vortices downstream of the two main vortices are formed at the time when the two main vortices detach from the cylinder and are thus a consequence of the change in boundary conditions at the body. The two main vortices enter the filtered region (which starts at x=10) around t=26 and figure (4b) shows the vortices after they have entered the filtered region. Figure (4c) shows the vortices when they are well inside the filtered region and are approaching the outflow boundary. Subsequent figures (d) and (e) show the vortices exiting the computational domain very cleanly without any apparent distortions. The only noticeable change in the shape of the vortices as they approach the outflow boundary is a stretching of the downstream portion of the vortices. This is mainly due to the pressure filter since the normal viscous term is typically quite small in this region and so the viscous filter has less of an effect than the pressure filter.

A more quantitative assessment of the performance of the outflow boundary condition can be made by computing the L_2-norm of the vorticity, $\|\omega_z\|_2 = \left[\int_\Omega \omega_z^2 dx dy\right]^{1/2}$. This quantity is a good indicator of how far the flow is from potential flow. Figure (5) shows this quantity plotted versus time. It can be seen that the norm of the vorticity decreases smoothly at a relatively slow rate up to around t=39. This decrease is due to the viscous dissipation of the vortices as they move downstream. The fact that vorticity decreases smoothly without any large change in its decay rate as the vortices enter the filtered region at $t \approx 26$ clearly shows that there is no generation of spurious vorticity as the vortices enter the filtered region.

At around t=39, the downstream end of the vortices starts to exit the outflow boundary and the vortices exit the computational domain completely at around t=42.4. During this period as expected, there is a rapid drop in vorticity. Apart from a small kink at around t=41.6 the drop in vorticity is smooth and seems to indicate that the vortices exit the domain without any reflection. The kink at t=41.6 corresponds to the rear end of the vortices exiting the computational domain. As can be noticed from the contour plot in figures (4c,d), the vorticity gradient in the rear end of the vortices is much larger than that at the front end of the vortices. The kink at t=41.6 is formed as a result of the boundary condition trying to adjust to the large gradient at the rear end of the vortices. This relatively large vorticity gradient at the upstream side of the vortices seems peculiar to the flow simulated in this test run and was not noticed in the actual simulations. Moreover, in the actual

simulations, the outflow boundary is farther away from the cylinder than it is in this simulation, thus we expect the vorticity gradients to be much smaller at the boundary.

It should also be pointed out that the norm of the vorticity in the computational domain drops by about one order of magnitude when the vortices exit the domain and then slowly reduces further over time. The fact that there is some residual vorticity in the domain even after the vortices have exited the domain is not due to any reflections at the outflow boundary, rather, it is due to the perturbations in the flow caused by the passage of the vortices, the effects of which persists even after the vortices themselves have exited the computational domain. Thus, it is not expected that the flow will return to potential flow immediately after the vortices have left the computational domain. The presence of the cylinder also adds to the slow return of the flow to potential, since, as long as the flow is not exactly potential there will be a vorticity layer, albeit small, on the cylinder.

The above test run then, gives us a lot of confidence in the capability of the boundary condition to convect large disturbances out without any significant reflections. As a final note, it should be reiterated that spectral methods are notoriously intolerant to inconsistent boundary conditions[15] and the fact that the current outflow boundary conditions work well in conjunction with these spectral simulations, further attests to the overall non-reflective nature of the boundary conditions.

CASE I(a) ($\mathcal{T}$=0.197, α=45°, Re=115)

Here the startup of the shedding process will be considered and this case has been chosen so that direct comparison can be made with numerical results published previously by Lugt & Haussling[8] (henceforth referred to as LH). In LH the length scale used is the focal length of the elliptic cylinder, therefore, when converted to our length scale, results in a factor of 1.73 both in the Reynolds number as well as the non-dimensional time scale. In figure (6) the vorticity contours at various stages of the startup process have been plotted (figures (6a,b,c) can be compared to figures (10e), (11c) and (11e) respectively in LH). When the results are compared with those in LH it is observed that even though qualitatively very similar vortex structures are observed, the startup process in our simulations seems to lag slightly behind that in LH.

A possible cause for the time lag could be the error arising from the *ad-hoc* intermediate velocity and pressure boundary conditions which are applied as part of the time-split procedure. To verify this hypothesis we have formulated the time-split scheme in such a way as to satisfy the no-slip condition exactly and also to apply the correct boundary condition for pressure on the body. The influence-matrix technique mentioned earlier (also described in the appendix) has been employed to derive boundary conditions for the intermediate velocities and pressure such that boundary conditions given by (27) are satisfied. Thus, the final flow satisfies boundary conditions which are totally consistent with the full Navier-Stokes equations.

Using the above technique the startup process has been simulated but it has been observed that there is no noticeable difference in the solution. A closer look at quantities like surface pressure and

vorticity shows no significant differences between the two simulations. Thus, the startup process still seems to lag behind that in LH. A useful conclusion we can make from this exercise is that for this flow, the *ad-hoc* boundary conditions (25) and (26) perform as well as the exact boundary conditions. Thus, even though the new method does not seem to gain much for the present simulations, it represents a methodology which might prove to be an attractive alternative for flow configurations where conventional coupled methods are difficult to apply (like variable viscosity problems) and where splitting errors introduced by *ad-hoc* boundary conditions may be unacceptable (like boundary driven flows).

Quantities of engineering interest like lift, drag and moment coefficients depend critically on the accurate computation of pressure on the cylinder surface. Pressure computed from the time-split procedure, both with and without the influence matrix method, suffers from operator splitting error. Keeping this in mind, it has been decided to base the lift, drag and moment coefficients on a pressure calculated using the correct pressure Poisson equation and boundary condition on the body, ie.

$$\nabla^2 P_c = -\nabla . \left[\boldsymbol{NL}(\boldsymbol{u}^{n+1}) \right] \quad in \ \Omega \tag{45}$$

$$\nabla P_c . \tilde{\tau}_\xi = \frac{1}{\mathrm{Re}} \boldsymbol{D}(\boldsymbol{u}^{n+1}) . \tilde{\tau}_\xi \quad on \ \partial\Omega_E \tag{46}$$

where P_c refers to the "correct" pressure computed using the above equation. Note that (45) is obtained by taking the divergence of the momentum equation (Eq. (4)) and (46) is simply the ξ-momentum equation evaluated on the cylinder. It should be stressed here that this pressure can not be made part of the time-stepping scheme and can only be obtained *a-posteriori.*

Surface variations of P and P_c at t=0.844 are plotted in figure (7) for comparison. It can be observed that the difference between P and P_c is small and is most observable in the region of the leading-edge separation point (near $\eta=\pi$). This reemphasizes the conclusion that for the present simulations, the time-split scheme with homogeneous Neumann pressure boundary condition does predict the correct pressure with reasonable accuracy.

Finally, since the influence matrix technique does not give results significantly different from the original formulation, we have opted to stay with our original time-split scheme. The force and moment coefficients however are based on the *a-posteriori* pressure P_c. Furthermore, the lift, drag and moment coefficients are defined as $C_L = \dfrac{L}{\frac{1}{2}\varrho U_\infty^2 2L_y L_z}$; $C_D = \dfrac{D}{\frac{1}{2}\varrho U_\infty^2 2L_y L_z}$ and $C_M = \dfrac{M}{\frac{1}{2}\varrho U_\infty^2 2L_y 2L_x L_z}$ where L, D and M are respectively the lift, drag and moment on the cylinder and ϱ is the density of the fluid.

CASE I(b) ($\mathcal{T}$=0.2, α=45°, Re=100)

This case is with parameters similar to those of CASE I(a) but here we present results of the fully developed periodic flow obtained after long time integration. Figures (8) and (9) show the pressure

and spanwise vorticity contours respectively at t=65 and a well defined Karman vortex street is clearly visible in both these figures. Looking at the pressure contours in figure (8) it is readily apparent that the CW vortex (vortex with clockwise rotation) is of much smaller strength and size than the CCW vortex (vortex with counter clockwise rotation). Figure (9) suggests that the strength of the shed vortices is directly related to the distance for which the vorticity layer remains attached to the body before separating and curling up into a vortex; the larger the distance, more is the amount of vorticity pumped into the vortex. Thus, the relative strength of the vortices depends primarily on the angle-of-attack and to a lesser extent on the thickness ratio. Figure (10) shows the variation of pressure over time at four locations near the cylinder (the locations have been tagged in figure (8)) and it can be seen that the flow has reached a fully developed periodic state.

Figure (11) shows the power spectral density corresponding to these pressure fluctuations plotted against the Strouhal number (St). The Strouhal number has been based on the thickness of the cylinder and the freestream velocity and is defined as $St = \mathcal{F} \cdot 2L_y/U_\infty$ where $\mathcal{F}$ is the frequency of oscillations. We also define a Strouhal number and Reynolds number based on the projected width (L^*), ie. the width of the cylinder "seen" by the flow, as $St^* = \frac{\mathcal{F}L^*}{U_\infty}$ and $\mathrm{Re}^* = \frac{L^*U_\infty}{\nu}$ where given a thickness ratio and angle-of-attack, L^* can be calculated analytically. The above Strouhal number can be used for comparison between flows over elliptic cylinders of various thickness ratios and angles-of-attack at the same Re^*. In particular, St^* can be compared with the corresponding Strouhal number for flow over circular cylinders in order to validate our results. Note that St^* is not strictly the universal Strouhal number[34] since it is not based on the actual wake width and velocity of the separated shear layer. Thus, it is not appropriate to compare St^* with the universal Strouhal number for flow over circular cylinders. It should be pointed out that for a zero angle-of-attack $St \equiv St^*$. Finally for the present case, Re^*=163.

The power spectrum shows one main peak corresponding to St=0.046 and a secondary peak corresponding to the first super-harmonic of this fundamental frequency. St^* corresponding to the fundamental frequency is 0.19 which compares very well with the value for flow over circular cylinders at the same Re^*. Published experimental results[2] estimate this value to between 0.17 and 0.19. Also it should be noted that no lower secondary frequency can be observed. Reflections from the outflow boundary have been known to cause spurious secondary frequencies[16]. Thus the absence of a secondary frequency for this relatively low Reynolds number flow, further establishes the effectiveness of the non-reflective outflow boundary condition.

Finally, figure (12) shows the streamline pattern corresponding to t=65. It shows a fully developed CCW vortex and a CW vortex in the early stage of its development.

CASE II ($\mathcal{T}$=0.5, α=0°, Re=1000)

This case is of flow over an elliptic cylinder of moderate thickness at a relatively high Reynolds number (Re^*=1000). Figure (13) shows the variation of the lift, drag and moment coefficients with time. Although an underlying periodicity is observed both in the lift and moment coefficients, there is a marked increase towards chaotic behavior. There is also a small drift in the average level of the drag coefficient which may indicate that there may be some transient effects still present in the flow. The average drag coefficient is in the range 0.6-0.7 which can be compared with a value of 0.6 obtained by Delaney & Sorenson[35] for an ellipse with $\mathcal{T}$=0.6, α=0° and Re=10^5.

Figure (14) shows the power spectra for the lift and drag variations. A fundamental frequency corresponding to a Strouhal number of 0.2 is observed for lift. The Strouhal number matches well with experimental results of Modi & Wiland[36] who measured a Strouhal number of 0.213 for a cylinder with $\mathcal{T}$=0.6, α=0° and Re=10^4-10^5. Also for comparison, the Strouhal number for flow over a circular cylinder at this Reynolds number has been established to be in the range 0.21-0.22[2].

CASE III ($\mathcal{T}$=0.5, α=45°, Re=300)

This case is of flow over an elliptic cylinder of moderate thickness at a high angle-of-attack and moderate Reynolds number (Re^*=525). The primary frequency computed from the time variations of the force and moment coefficients corresponds to St=0.14. For comparison, Modi & Wiland[36] measured a Strouhal number of 0.143 for a ellipse with $\mathcal{T}$=0.6, α=45° and Re=10^4-10^5. The corresponding Strouhal number based on the projected width is computed as St^*=0.24 which is higher than the corresponding value for a circular cylinder which is about 0.21[2]. This seems to indicate that for this case, L^* overestimates the width of the wake. Finally it should be pointed out that no low secondary frequencies are observed for this case as well.

It was decided to investigate the effect of the size of the domain on the computed flow field. The domain independence study has significance here in that it evaluates the effect that the outer boundary condition has on the overall dynamics of the flow. Spectral simulations of flow over circular cylinders have shown that the frequency of shedding can be dependent on the size of the domain and the type of boundary condition used at the outer boundary[1]. The outer computational domain was reduced from 40 to 30 length units and to maintain roughly the same time-step size and maximum CFL number, the number of grid points was also reduced to N_ξ=81 and N_η=100. The flow was then started with the initial potential condition and allowed to evolve in time. When computed force and moment coefficients are compared with the corresponding results obtained in the larger domain, no noticeable differences are observed. Furthermore, the Strouhal number corresponding to the shedding frequency also comes out to be 0.14 which matches exactly with the Strouhal number obtained for the simulation in the larger domain. Thus, the results of the simulations are insensitive to the domain size and provide further evidence of the effectiveness of the inflow and outflow boundary conditions.

3-D Simulation

$\mathcal{T}$=0.5, A=2.0, $\alpha=45^0$, Re=300

The parameters chosen for the 3-D simulation are the same as those for the Case III in the 2-D simulation study. Flow over a circular cylinder has been observed to become three-dimensional beyond a Reynolds number of about 180 [1,37] and we expect that the flow around elliptic cylinders will also behave qualitatively in a very similar manner. Thus we hope to see a significant three-dimensional wake structure at Re=300 (Re^*=525). Also it has been observed by Williamson[3] that the wavelength of the spanwise structures in the wake of a circular cylinder at these Reynolds numbers is typically about one length unit. Thus an aspect ratio of two for the present simulation should be just about equal to the correlation length in that direction. This smaller spanwise aspect ratio allows us to have relatively few grid points in the spanwise direction and thus this preliminary 3-D run can be performed cheaply. Subsequent 3-D runs will be done with a larger spanwise aspect ratio. The 3-D simulation is performed in the smaller domain ($x_O = 30$) with a 81x100x28 grid. It should be pointed out that the objective of this 3-D simulation is primarily to test the performance of the 3-D solver and to showcase the richness of the flow structure in the near wake that is exhibited even at this low Reynolds number.

The above simulation requires about 6.5μs per time step per grid point on the C-90 (1 CPU). For this grid that amounts to about 1.5 seconds per time step. The maximum allowable time step size is limited by the CFL criterion and is $2x10^{-3}$ for this simulations, thus requiring about 1.5 hours of CPU time to simulate one Karman vortex shedding cycle. The 3-D run is initiated by perturbing a fully developed 2-D flow and it takes about 5-6 shedding cycles for the flow to reach a fully developed 3-D state. Thus, the total time required for one such simulation is between 10-15 hours of CPU time on the C-90. It should be pointed out that the CFL criterion is more restrictive for flows at high angles-of-attack and typically the time step size can be increased by a factor of 2 to 5 for simulating flows at lower angles-of-attack.

Figure (15) shows isosurfaces of spanwise vorticity when the three-dimensionality is well developed(t=102.5). One can see that there is substantial variation in the structure of the rollers along the spanwise direction. In particular, the attached CW roller shows large variations in the spanwise direction. In figure (16) we have plotted the isosurface corresponding to ω_z=-3.0 and one can clearly see the cup-like regions of concentrated spanwise vorticity associated with the CW roller. These are very similar to the kind of structures found by Moser & Rogers[38] in mixing layers.

In figure (17) are plotted isosurfaces of streamwise vorticity and rib-like vortex structures can be seen clearly. It is interesting to note that large ribs are located in the braid region of the CW roller whereas the ribs associated with the CCW rollers are much smaller. This may be because the strain field that is responsible for the generation of streamwise vorticity, is more intense in the braid region

of the CW rollers. A study of the topological features and the interaction of these vortex structures is currently in progress.

CONCLUSIONS

The solver developed for the simulation of flow over elliptic cylinders is an efficient one in terms of both the CPU and memory requirement and will allow us to make a comprehensive analysis of the various aspects of the 3-D flow field. The outflow boundary conditions have been handled by parabolizing the governing equations near the outflow boundary and the issues in the implementation of this technique have been discussed in detail. In particular, general guidelines have been proposed that should help the implementation of this technique in other similar flows. In addition to this, a novel inflow boundary condition is also proposed that allows for the blockage effect of the body to be "felt" in the inflow portion of the outer computational boundary. It has been demonstrated that this boundary condition improves the overall behavior of the solution.

Our simulation of the startup process show a time-lag when compared to the results in LH. The reason for this discrepancy is not clear at this time. A possible source of error, namely inconsistent boundary conditions, has been eliminated by using a new technique in conjunction with a two-step time-split scheme whereby the exact pressure and velocity boundary conditions are imposed on the body. However, this does not change the results in any significant way. The conclusion is that the conventional boundary conditions for the time-split method perform as well as the exact boundary conditions for this flow.

A number of 2-D simulations have been performed and quantities like Strouhal numbers and drag coefficients show good agreement with established experimental results. A preliminary 3-D simulation has also been performed at a relatively low Reynolds number (Re=300). A rich three-dimensional wake structure is observed and vortex structures including rollers with large spanwise variations, cup-like structures of concentrated spanwise vorticity and rib-like structures of concentrated streamwise vorticity are observed. Similar structures have been observed in the DNS of mixing layers[38]. Despite the above similarity, it is observed that the asymmetry of the wake for an elliptic cylinder at an angle-of-attack has a significant effect on the topology of the vortex structures and leads to a flow structure different from symmetric flows like circular cylinder wakes and mixing layers. A study of the implications this has on mixing and transition to turbulence is currently underway.

ACKNOWLEDGEMENTS

These computations have been performed on the Cray-YMP at National Center for Supercomputing Application at the University of Illinois at Urbana-Champaign and on the C-90 at

the Pittsburg Supercomputing Center. Financial support for this work has been provided by Schlumberger Technical Corporation under the Industrial Supercomputing Program Agreement.

APPENDIX

Removal of Splitting Errors for a Two-Step Time-Split Scheme

A technique similar to the one used by Marcus[26] is used to impose the exact boundary conditions on the elliptic cylinder for a two-step time-split scheme. For the sake of simplicity, the discussion in this appendix will be restricted to two dimensions since extension to three dimensions involves no additional complications. Also, since this method is aimed towards improving the boundary conditions on the surface of the cylinder, boundary conditions at the outer boundary will be assumed to be known.

The influence-matrix technique reduces to identifying the correct wall-normal (α) and tangential velocity (β) boundary conditions which when enforced at the intermediate (*) level will result in no-slip and no penetration at the end of the full time-step with the additional condition that the pressure satisfy the normal momentum equation at the body. The equations and boundary conditions solved at the intermediate step can be written as follows:

$$\mathcal{M}_b u^* = R_\xi \quad in\ \Omega\ ; \qquad u^*(\xi_E,\eta_j) = \alpha_j \quad on\ \partial\Omega_E \tag{47}$$

$$\mathcal{M}_b v^* = R_\eta \quad in\ \Omega\ ; \qquad v^*(\xi_E,\eta_j) = \beta_j \quad on\ \partial\Omega_E \tag{48}$$

where $\mathcal{M}_b$ is the linear operator appearing on the LHS of Eq. (21), R_ξ and R_η are the wall-normal and azimuthal components of the right hand side. Inflow and outflow conditions are enforced on $\partial\Omega_O$. This advection diffusion step is followed by the pressure correction step

$$\nabla^2 P^{n+1} = f(\xi,\eta)\frac{\nabla . \boldsymbol{u}^*}{\Delta t} \quad in\ \Omega\ ; \qquad \nabla P^{n+1}(\xi_E,\eta_j) . \tilde{\tau}_\xi = \frac{\alpha_j}{\Delta t} \quad on\ \partial\Omega_E \tag{49}$$

$$\boldsymbol{u}^{n+1} = \boldsymbol{u}^* - \Delta t \nabla P^{n+1} \quad in\ \Omega + \partial\Omega \tag{50}$$

The Neumann boundary condition for the pressure Poisson equation along with the pressure correction (Eq. (50)) guarantee impermeability ($u^{n+1} = 0$) on the surface of the cylinder. As before, at the outer boundary $\nabla P^{n+1} . \tilde{\tau}_\xi = 0$. Now α's and β's will be chosen so that the resulting final velocity and pressure satisfy the no-slip condition and the wall-normal momentum equation at the body, given by

$$u^{n+1} = 0 \quad \text{and} \quad \nabla P^{n+1} . \tilde{\tau}_\xi = \frac{1}{\mathrm{Re}} \nabla^2 \boldsymbol{u}^{n+1} . \tilde{\tau}_\xi \quad on\ \partial\Omega_E \tag{51}$$

Let the set of equations (47)-(50) be called the "A-problem." Since the functions α and β are unknown *a-priori* in the calculation of u^* and v^*, the above A-problem cannot be solved directly. This difficulty can be avoided by using the influence matrix technique, where instead of solving the above A-problem, one solves for a particular solution (B-problem) and two sets of complementary functions (C-problem and D-problem). The particular solution (u_B, v_B, P_B) is obtained by solving

(47)-(50) with homogeneous boundary conditions $u^* = v^* = \nabla P^{n+1} . \tilde{\tau}_\xi = 0$ applied on the cylinder. Each member of the first set of complimentary functions (u_C, v_C, P_C) is obtained as response to a unit source of intermediate wall normal velocity placed at one point on the cylinder surface. Different members of the first set are thus built by placing the wall-normal velocity source at all the points on the cylinder surface one at a time. Thus, there are as many C-complimentary functions as there are number of points along the η directions ie. N_η. The equations solved for the j^{th} C-problem then are

$$\mathcal{M}\mathfrak{o} u^*_{C_j} = 0 \quad in \ \Omega \ ; \qquad u^*_{C_j}(\xi_E, \eta_l) = \delta_{jl} \ on \ \partial\Omega_E \tag{52}$$

$$\mathcal{M}\mathfrak{o} v^*_{C_j} = 0 \quad in \ \Omega \ ; \qquad v^*_{C_j}(\xi_E, \eta_l) = 0 \ on \ \partial\Omega_E \tag{53}$$

$$\nabla^2 P_{C_j} = f(\xi,\eta)\frac{\nabla . \boldsymbol{u}^*_{C_j}}{\Delta t} \quad in \ \Omega \ ; \qquad \nabla P_{C_j}(\xi_E, \eta_l) . \tilde{\tau}_\xi = \frac{\delta_{jl}}{\Delta t} \ on \ \partial\Omega_E \tag{54}$$

$$\boldsymbol{u}^{n+1}_{C_j} = \boldsymbol{u}^*_{C_j} - \Delta t \nabla P_{C_j} \quad in \ \Omega + \partial\Omega \tag{55}$$

Here the boundary conditions for the j^{th} C-problem imply a unit wall normal velocity at the j^{th} η-point and zero wall normal velocity at all other wall points. A corresponding wall normal pressure gradient is also enforced at this point to ensure zero penetration at the end of the full time step. The D-complementary functions can be obtained in a similar fashion where the solution of the j^{th} D-problem will be obtained by applying a unit tangential slip at the $j^{th}\eta$-point on the cylinder surface at the $(^*)$ level. The D-complementary functions satisfy no penetration at all the η-points automatically. The solution for the A-problem can then be written as a linear combination of the particular and complimentary solutions as

$$\begin{bmatrix} u^{n+1} \\ v^{n+1} \\ P^{n+1} \end{bmatrix} = \begin{bmatrix} u^{n+1}_B \\ v^{n+1}_B \\ P_B \end{bmatrix} + \alpha_j \begin{bmatrix} u^{n+1}_{C_j} \\ v^{n+1}_{C_j} \\ P_{C_j} \end{bmatrix} + \beta_j \begin{bmatrix} u^{n+1}_{D_j} \\ v^{n+1}_{D_j} \\ P_{D_j} \end{bmatrix} \tag{56}$$

Here the unknown coefficients α's and β's are just the appropriate wall normal and tangential velocity boundary values that will enable the overall velocity and pressure to satisfy (51). The algebraic relation for the α's and β's can be written in the following matrix form:

$$\begin{bmatrix} v^{n+1}_{C_j} & v^{n+1}_{D_j} \\ \left(\nabla P_{C_j} - \frac{1}{\mathrm{Re}}\nabla^2 \boldsymbol{u}^{n+1}_{C_j}\right) . \tilde{\tau}_\xi & \left(\nabla P_{D_j} - \frac{1}{\mathrm{Re}}\nabla^2 \boldsymbol{u}^{n+1}_{D_j}\right) . \tilde{\tau}_\xi \end{bmatrix} \begin{pmatrix} \alpha_j \\ \beta_j \end{pmatrix} = \begin{bmatrix} -v^{n+1}_B \\ -\left(\nabla P_B - \frac{1}{\mathrm{Re}}\nabla^2 \boldsymbol{u}^{n+1}_B\right) . \tilde{\tau}_\xi \end{bmatrix} \tag{57}$$

The vector on the RHS corresponds to the final slip error and normal momentum residual in the particular solution due to the imposition of *ad-hoc* homogeneous intermediate boundary conditions. The matrix on the left hand side is the influence matrix, whose elements represent the slip error and normal momentum residual at every point on the body due to placement of a unit penetration or slip source at a point on the surface. Solution of the above matrix equation provides the correct

combination of complimentary functions that nullifies the slip velocity and normal momentum residual produced at the cylinder by the particular solution. Thus the advection-diffusion and pressure correction steps in the A-problem become decoupled and the problem can be solved with the correct intermediate boundary conditions.

Once α's and β's are computed by solving (57), the final solution can be obtained in two different ways. The first option is to solve the A-problem with the correct intermediate boundary condition. Since the influence matrix can be computed once at the beginning and stored for repeated later use, the above option requires solving the momentum and pressure equation twice at each time step. The second option is to compute the final flow field using Eq. (56) which requires the storage of the two sets of complimentary functions in addition to the influence matrix. In a general case, this option could be prohibitively expensive in terms of computer memory, even though this requires that the momentum equations be solved only once every time step. However, the present explicit formulation of the η and z viscous terms simplify the complimentary functions and reduce their required storage to order $N_\xi N_\eta N_z$ thereby allowing us to store them once at the beginning of the run. Thus, only the pressure Poisson equation needs to be computed again at each time-step leading to an increase of at most 40% in the CPU time. Therefore, it seems that there is a distinct advantage in treating the tangential viscous terms explicitly when combined with this influence matrix technique.

Finally, there are some subtle points which make the implementation of the current influence-matrix technique different from that of Marcus[26]. These differences arise due to the fact that his implementation is for a three-step time-split scheme whereas the current implementation is in conjunction with a two-step time-split scheme. The three-step scheme advances the solution sequentially through advection, pressure correction and diffusion steps. For the three-step method, the intermediate velocity obtained after the pressure step satisfies the divergence-free condition. The final velocity after the diffusion step however, satisfies the no-slip and no-penetration conditions exactly but is not divergence free. Therefore instead of no-slip, the divergence-free condition at the boundary is used to construct the influence matrix. In contrast to this, in the present formulation, requiring zero boundary divergence of the final velocity leads to an ill-posed set of equations and results in explosive instability.

REFERENCES

1) Karniadakis, G.E., and Triantafyllou, G.E., Three-Dimensional Dynamics and Transition to Turbulence in the Wake of Bluff Objects, *J. Fluid. Mech.*, **238**, 1-30, 1992.

2) Roshko, A., On the Development of Turbulent Wakes from Vortex Streets, NACA Rep. 1191, 1954.

3) Williamson, C.H.K., The Natural and Forced Formation of Spot-Like 'Vortex Dislocations' in the Transition of a Wake, *J. Fluid Mech.*, **243**, 393-441, 1992.

4)Proudman, I., and Pearson, J.R., Expansions at Small Reynolds Numbers for a Flow Past a Sphere and a Circular Cylinder, *J. Fluid Mech.*, **2**, 237-262, 1957

5) Wang, C-Y., The Flow Past a Circular Cylinder Which is Started Impulsively from Rest, *J. Math. Physics*, **46**, 195-202, 1967.

6) Jafroudi, H., Yang, H-T. and Hermel, J., Matched Asymptotic Solutions of Impulsive Flow over and Elliptic Cylinder, *J. Comp. Phys.*, **109**, 289-305, 1993.

7) Lugt, H.J., and Haussling, H.J., Laminar Flow Past Elliptic Cylinders at Various Angles of Attack, *Dept. of Navy, Naval Ship Research and Development Center Report* 3748, 1972.

8) Lugt, H.J., and Haussling, H.J., Laminar Flow Past an Abruptly Accelerated Elliptic Cylinder at 45^0 Incidence, *J. Fluid Mech.*, **65**, part 4, 771-734, 1974.

9) Blodgett, K.E.J., Unsteady Separated Flow Past an Elliptic Cylinder Using the 2-D Incompressible Navier Stokes Equations, *MS Thesis*, University of Cincinnati, 1989.

10) Canuto, C., Hussaini, M.Y., Quarteroni, A., and Zang, T.A. *Spectral Methods in Fluid Dynamics*, Springer-Verlag, New York, 1988.

11) Patera, A.T., A Spectral Element Method for Fluid Dynamics: Laminar Flow in a Channel Expansion, *J. Comp. Phys.*, **54**, 468-488, 1984.

12) Macaraeg, M., and Streett, C.L., Improvements in Spectral Collocation Through a Multiple Domain Technique, *Appl. Numer. Math.*, **2**, 95-108, 1986.

13) Streett, C.L., and Macaraeg, M., Spectral Multi-Domain for Large Scale Fluid Dynamic Simulations, *Appl. Numer. Math.*, **6**, 123-139, 1989.

14) Orszag, S.A., Spectral Methods for Problems in Complex Geometries, *J. Comp. Phys.*, **37**, 70-92, 1980.

15) Don, W.S., and Gottlieb, D., Spectral Simulation of Unsteady Compressible Flow Past a Circular Cylinder, NASA CR-182030, 1990.

16) Abarbanel, S.S., Don, W.S., Gottlieb, D., Rudy, D.H., Townsend, J.C., Secondary Frequencies in the Wake of a Circular Cylinder with Vortex Shedding, *J. Fluid Mech.*, **225**, 557-574, 1991.

17) Yanenko, N.N., *The Method of Fractional Steps for Solving Multi Dimensional Problems of Mathematical Physics in Several Variables,* ed. by M. Holt, Springer Berlin, Hiedelberg, New York, 1971.

18) Chorin, A.J., Numerical Solution of the Navier-Stokes Equations, *Math. Comput.*, **22**, 745-762, 1968.

19) Orszag, S.A., and Kells, L.C., Transition to Turbulence in Plane Poiseuille and Plane Couette Flow, *J. Fluid Mech.*, **96**, part 1, 159-205, 1980.

20) Kim, J., and Moin, P., Application of Fractional-Step Method to Incompressible Navier-Stokes Equations, *J. Comp. Phys.*, **59**, 308-323, 1985.

21) Orszag, S.A., Israeli, M., and Deville, M.O., Boundary Conditions for Incompressible Flow, *J. Sci. Comp.*, **1**, No. 1, 75-111, 1986.

22) Karniadakis, G.E., Israeli, M., and Orszag, S.A., High-Order Splitting Methods for the Incompressible Navier-Stokes Equations, *J. Comp. Phys.*, **97**, 414-443, 1991.

23) Tomboulides, A.G., Israeli, M. and Karniadakis, G.E., Efficient Removal of Boundary-Divergence Errors in Time-Splitting Methods, *J. Sci. Comp.*, **4**, No. 3, 291-308, 1989.

24) Perot, J.B., An Analysis of the Fractional Step Method, *J. Comp. Phys.*, **108**, 51-58, 1993.

25) Klieser, L., and Schumann, U., Treatment of Incompressibility and Boundary Conditions in 3-D Numerical Spectral Simulations of Plane Channel Flows, *Proc of 3rd GAMM Conf. on Numerical Methods in Fluid Mechanics,* ed. by Hirschel, E.H., 165-173, 1980.

26) Marcus, P.S., Simulation of Taylor-Couette Flow Part I Numerical Methods and Comparison with Experiments, *J. Fluid Mech.*, **146**, 45-64, 1984.

27) Streett, C.L. and Hussaini, M.Y., A Numerical Simulation of the Appearance of Chaos in Finite-Length Taylor-Couette Flow, *Appl. Numer. Math.*, **7**, 41-71, 1991

28) Grosch, C.E., and Orszag, S.A., Numerical Solution of Problems in Unbounded Regions: Coordinate Transforms, *J. Comp. Phys.*, **25**, 273-296, 1977.

29) Boyd, J.P., The Optimization of Convergence for Chebyshev Polynomial Method Methods in an Unbounded Domain, *J. Comp. Phys.*, **45**, 43-79, 1982.

30) Joslin, R.D., Streett, C.L., and Chang,C-H, Validation of Three-Dimensional Incompressible Spatial Direct Numerical Simulation Code-A Comparison With Linear Stability and Parabolic Stability Equation Theories for Boundary-Layer Transition on a Flat Plate, NASA TP 3205, 1992.

31) Streett, C.L., *Private Communication.*

32) Madabhushi, R.K., Balachandar, S., and Vanka, S.P., A Divergence-Free Chebyshev Collocation Procedure for Incompressible Flows with Two Non-Periodic Directions, *J. Comp. Phys.* **105**, 199–206, 1993.

33) Ku, H.C., Hirsh, R.S. and Taylor, T.D., A Pseudospectral Method for Solution of the Three-Dimensional Incompressible Navier-Stokes Equations, *J. Comp. Phys.*, **70**, 439-462, 1987.

34) Roshko, A., On the Wake and Drag of Bluff Bodies, *J. Aero Sci.*, **22**, 124-132, 1955.

35) Delaney, N.K., and Sorenson, N.E., Low-Speed Drag of Cylinders of Various Shapes, NACA TN 3038, 1953.

36) Modi, J. and Wiland, E., Unsteady Aerodynamics of Stationary Elliptic Cylinders in Subcritical Flow, *AIAA J.*, **8**, No. 10, 1814-1821, 1970.

37) Hama, F.R., Three-Dimensional Vortex Pattern Behind a Circular Cylinder, *J. Aero. Sci.*, **24**, 156-158, 1957.

38) Moser, R.D. and Rogers, M.M., Mixing and Transition to Small Scales in a Plane Mixing Layer, *Phys. Fluids* A **3** (5), 1128-1134, 1991.

Captions for the figures

Fig.(1) A representative 2–D computational grid.

Fig.(2) Schematic of the computational domain showing the various boundary conditions at the outer boundary.

Fig.(3) Comparison of perturbation velocities obtained at the outer boundary with Dirichlet and mixed inflow boundary conditions. ($\mathcal{T}$=0.5,$\alpha=0^0$,Re=1000). (a) u' variation at the outer boundary. (b) v' variation at the outer boundary.

Fig.(4) Sequence of vorticity contours as the two vortices convect downstream through the filtered region and exit at the outflow boundary.

Fig.(5) Variation of L_2 norm of vorticity with time.

Fig.(6) Vorticity contours obtained during the startup process ($\mathcal{T}$=0.197, $\alpha=45^0$, Re=115).

Fig.(7) Comparison of surface pressure obtained using the regular time–split method and the *a–posteriori* pressure at t=0.844.

Fig.(8) Contours of pressure at t=65.0 ($\mathcal{T}$=0.2, $\alpha=45^0$, Re=100).

Fig.(9) Contours of spanwise vorticity at t=65.0.

Fig.(10) Time variation of pressure at the four locations tagged in Fig.(8).

Fig.(11) Power spectrum of the pressure variations shown in Fig.(10).

Fig.(12) Streamline pattern corresponding to the instant in time for which pressure contours have been shown in Fig.(8).

Fig.(13) Time variation of the lift, drag and moment coefficients ($\mathcal{T}$=0.5, $\alpha=0^0$, Re=1000).

Fig.(14) Power spectrum of the lift, drag and moment coefficient variations shown in Fig.(17).

Fig.(15) Isosurfaces of spanwise vorticity (ω_z) at t=102.5 showing the 3–D Karman vortex street ($\mathcal{T}$=0.5, $\alpha=45^0$, Re=300, A=2).

Fig.(16) Single isosurface of spanwise vorticity (ω_z) at t=102.5.

Fig.(17) Isosurfaces of streamwise vorticity (ω_{sw}) at t=102.5.

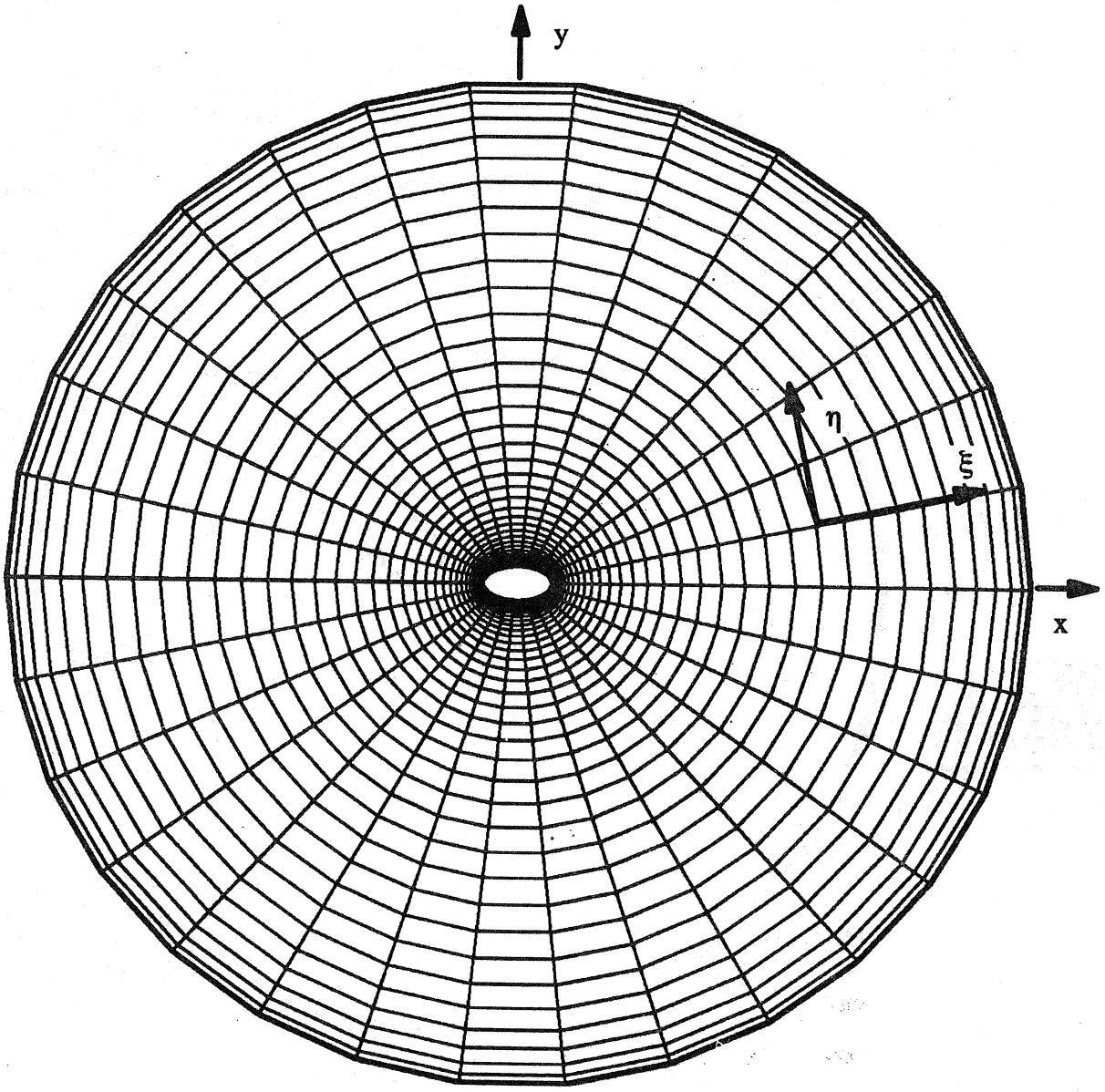

Fig. (1)

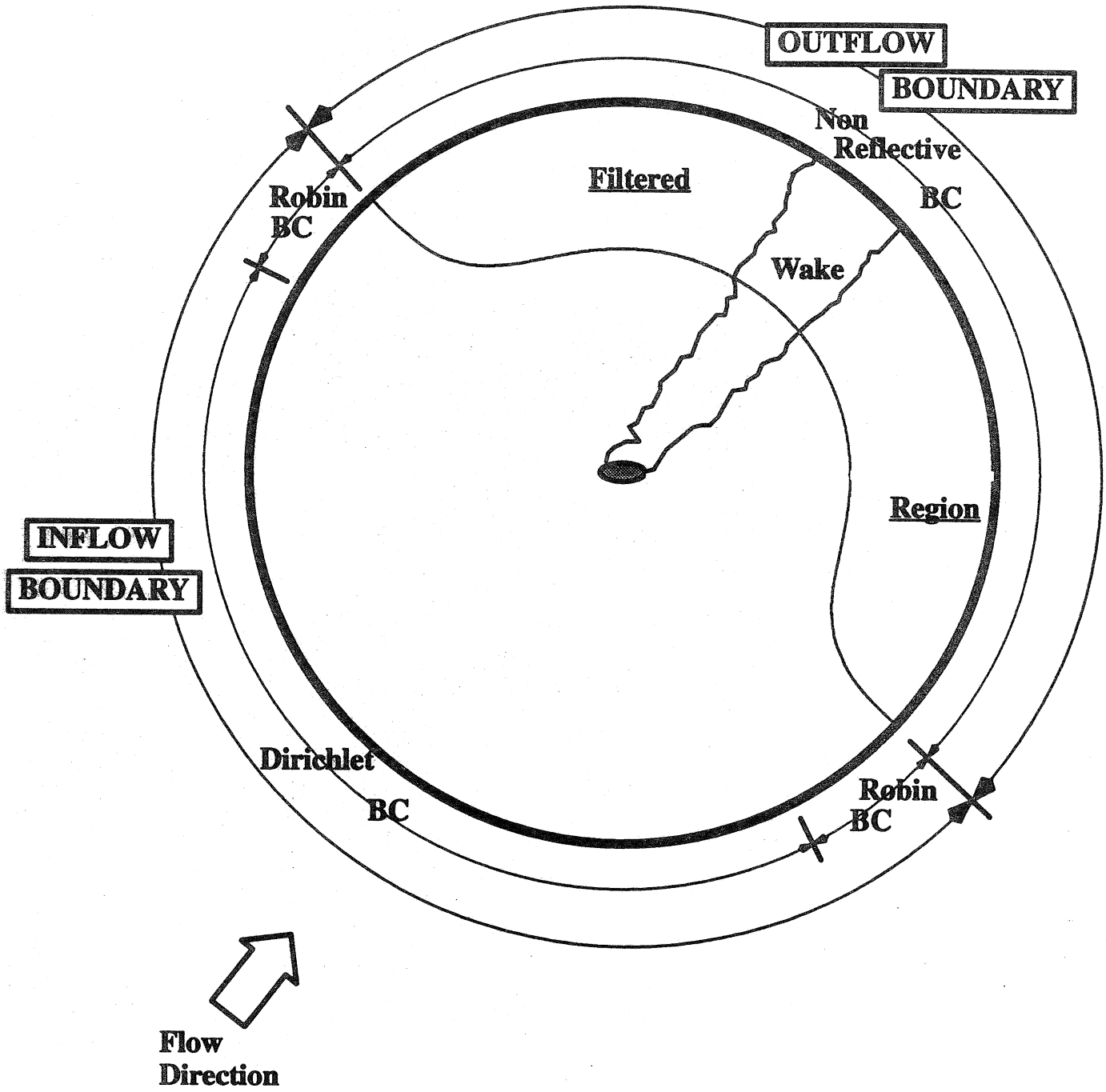
OUTFLOW
BOUNDARY
Non
Reflective
BC
Filtered
Robin
BC
Wake
Region
INFLOW
BOUNDARY
Dirichlet
BC
Robin
BC
Flow
Direction

Fig. (2)

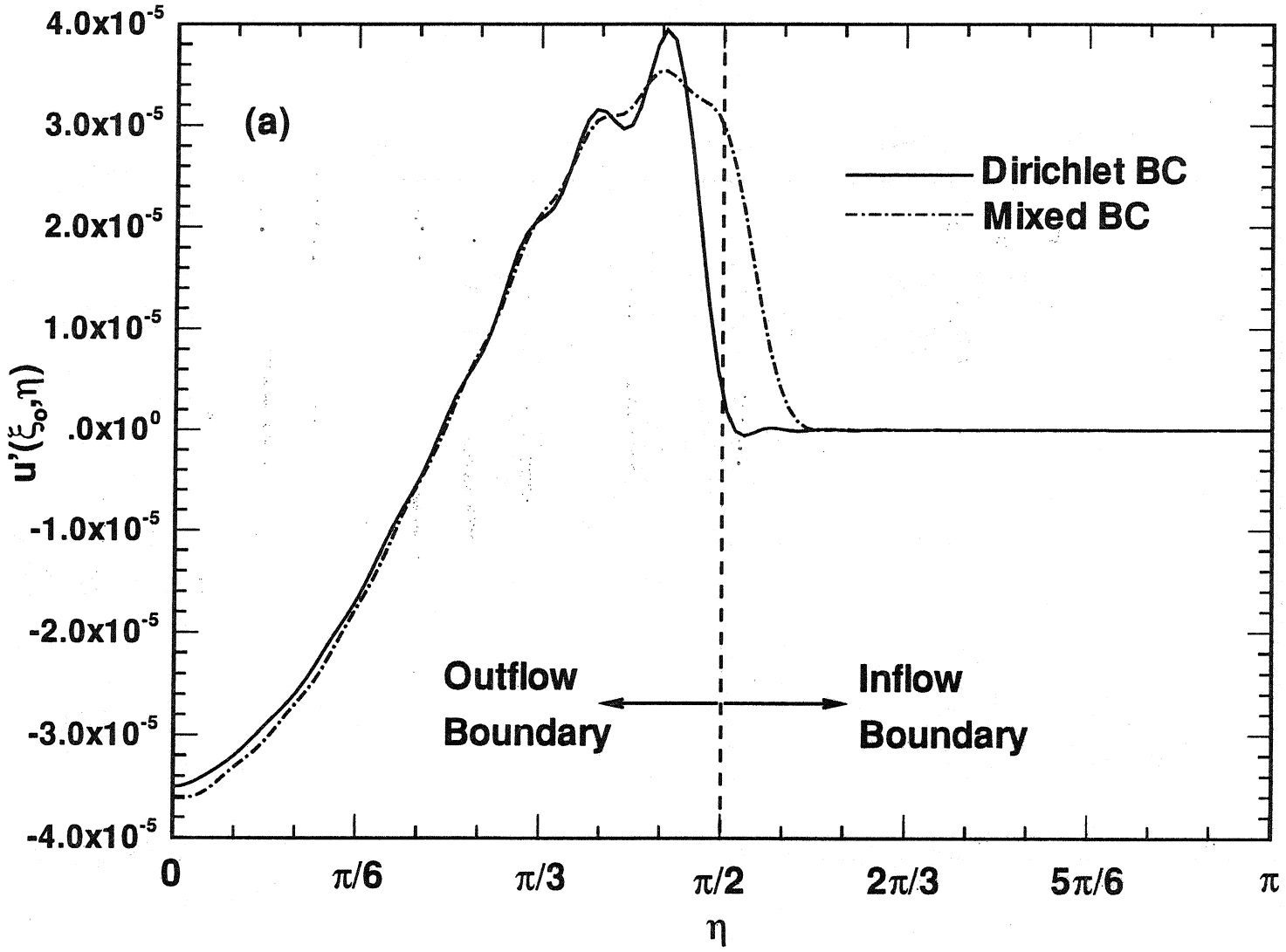
4.0x10-5
3.0x10-5
2.0x10-5
1.0x10-5
.0x100
-1.0x10-5
-2.0x10-5
-3.0x10-5
-4.0x10-5
u'(ξo,η)
(a)
Dirichlet BC
Mixed BC
Outflow
Boundary
Inflow
Boundary
0
π/6
π/3
π/2
2π/3
5π/6
π
η

Fig. (3a)

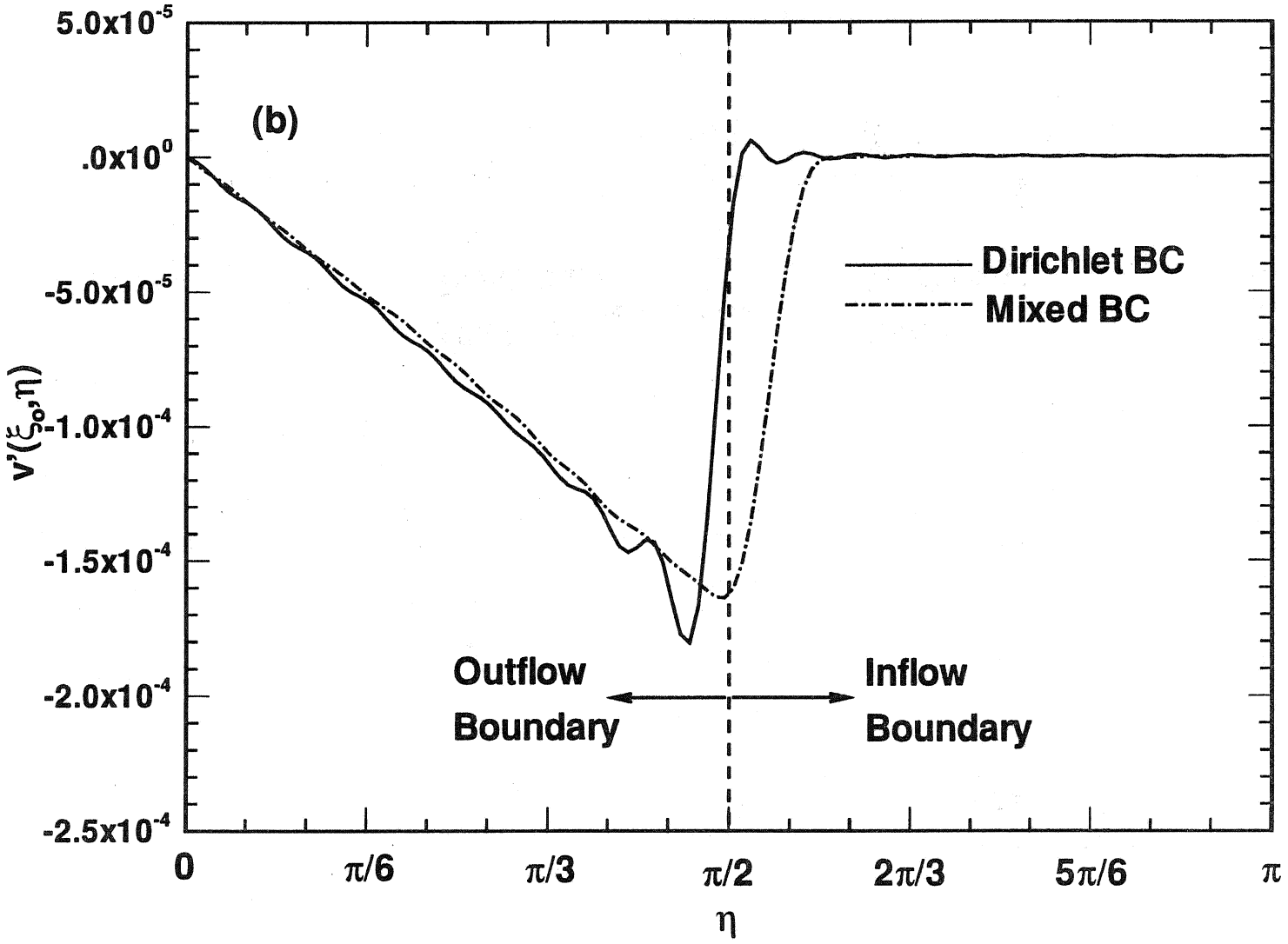
5.0x10^-5
.0x10^0
-5.0x10^-5
-1.0x10^-4
-1.5x10^-4
-2.0x10^-4
-2.5x10^-4
v'(ξo,η)
(b)
Dirichlet BC
Mixed BC
Outflow
Boundary
Inflow
Boundary
0
π/6
π/3
π/2
2π/3
5π/6
π
η

Fig. (3b)

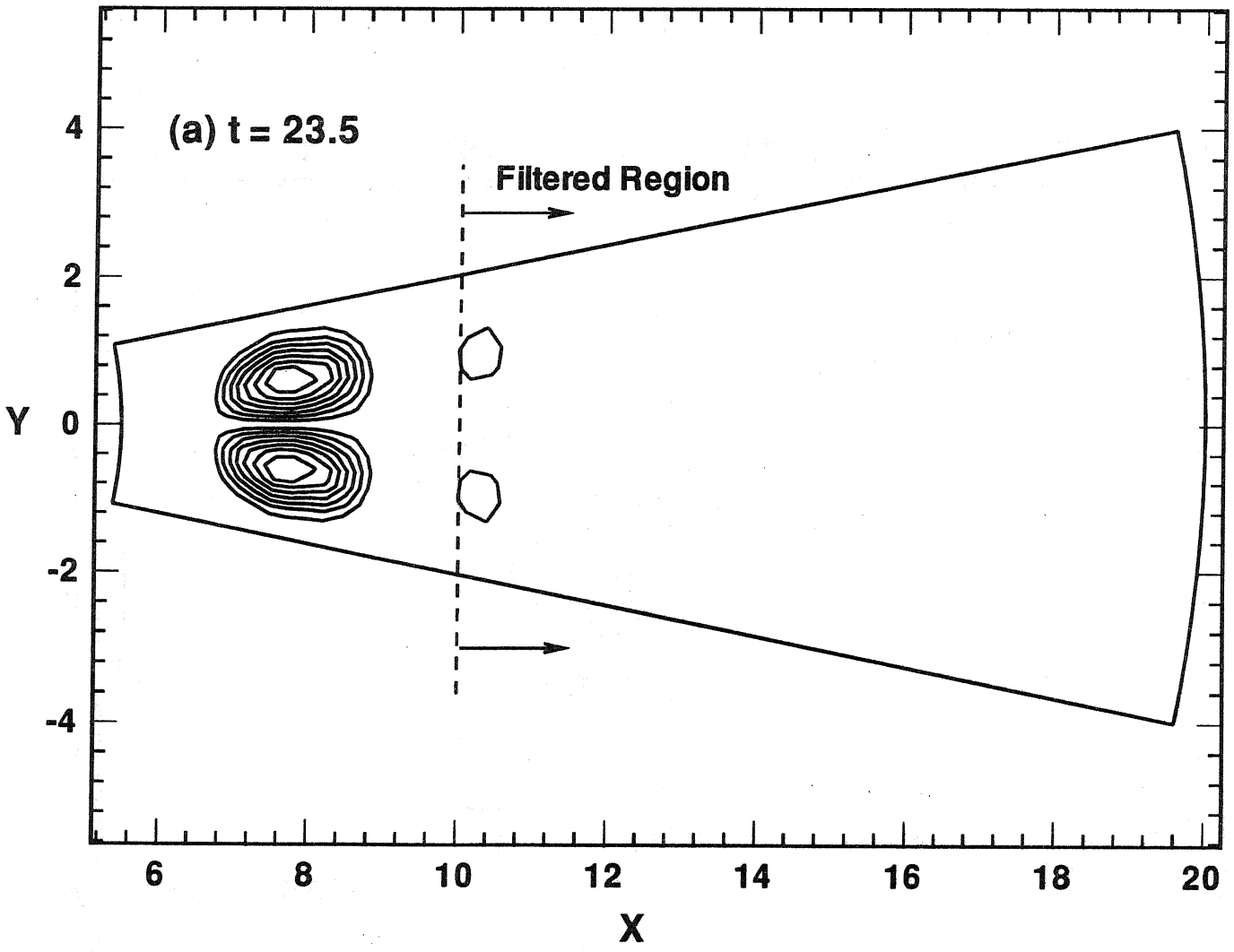

Fig. (4a)

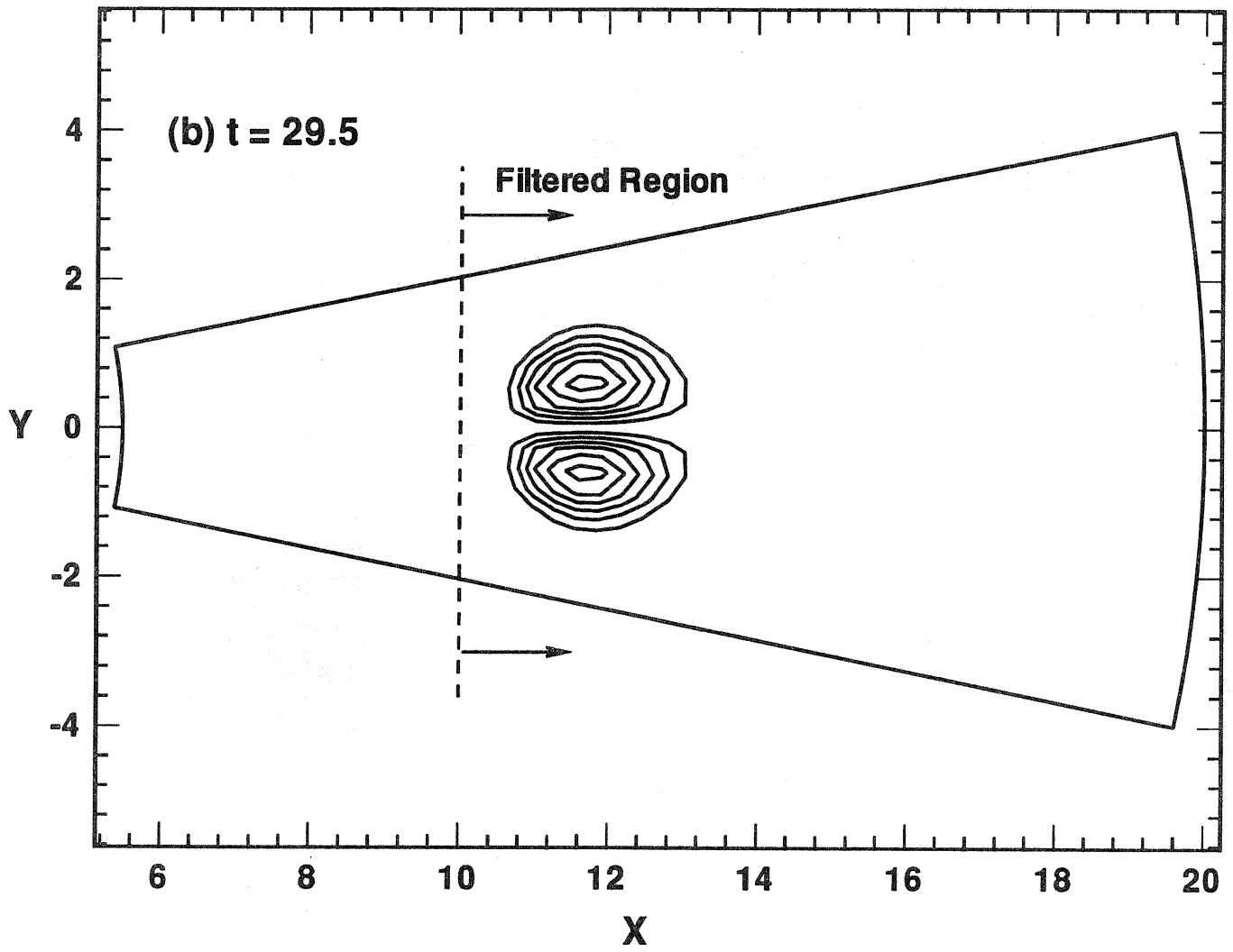

Fig. (4b)

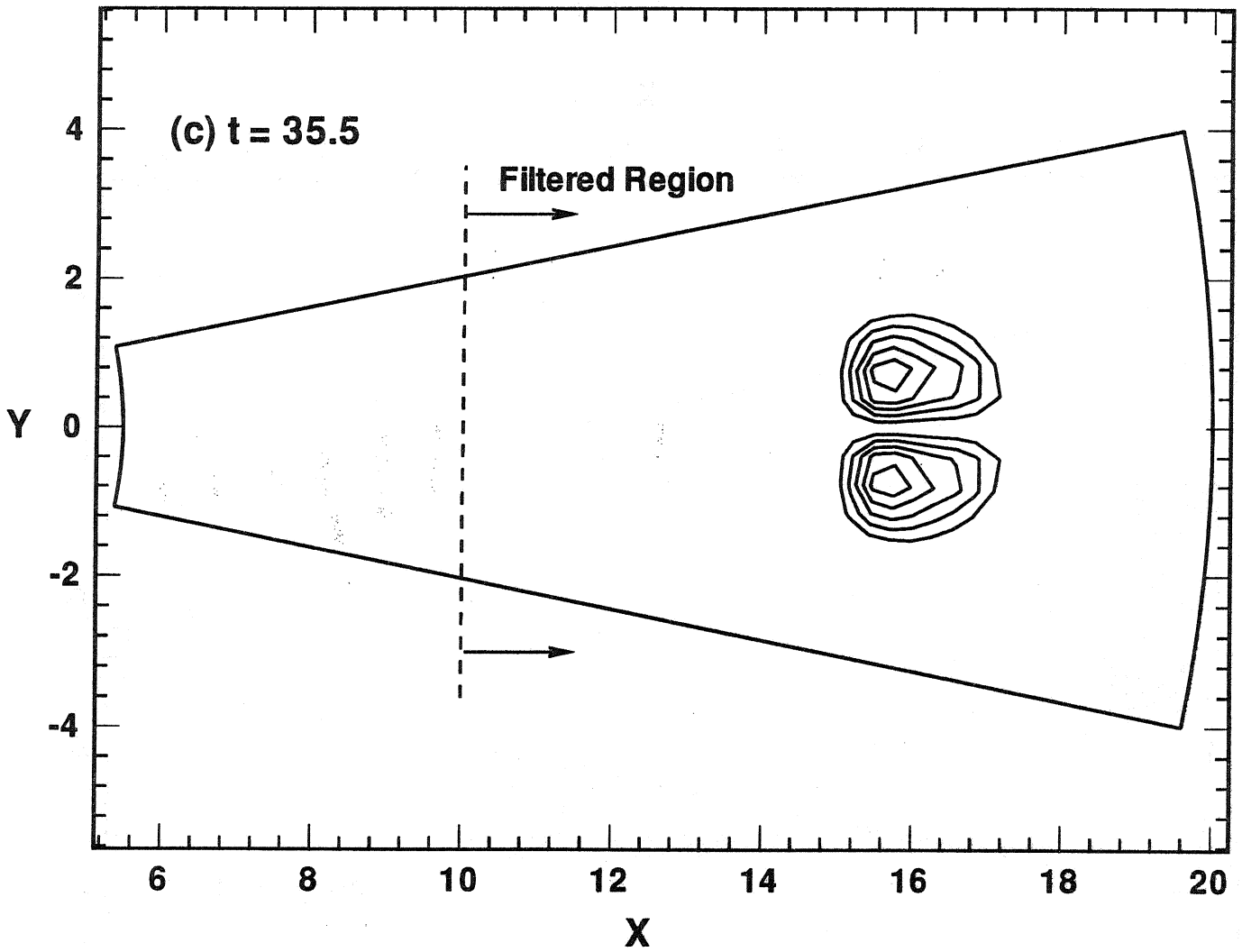

Fig. (4c)

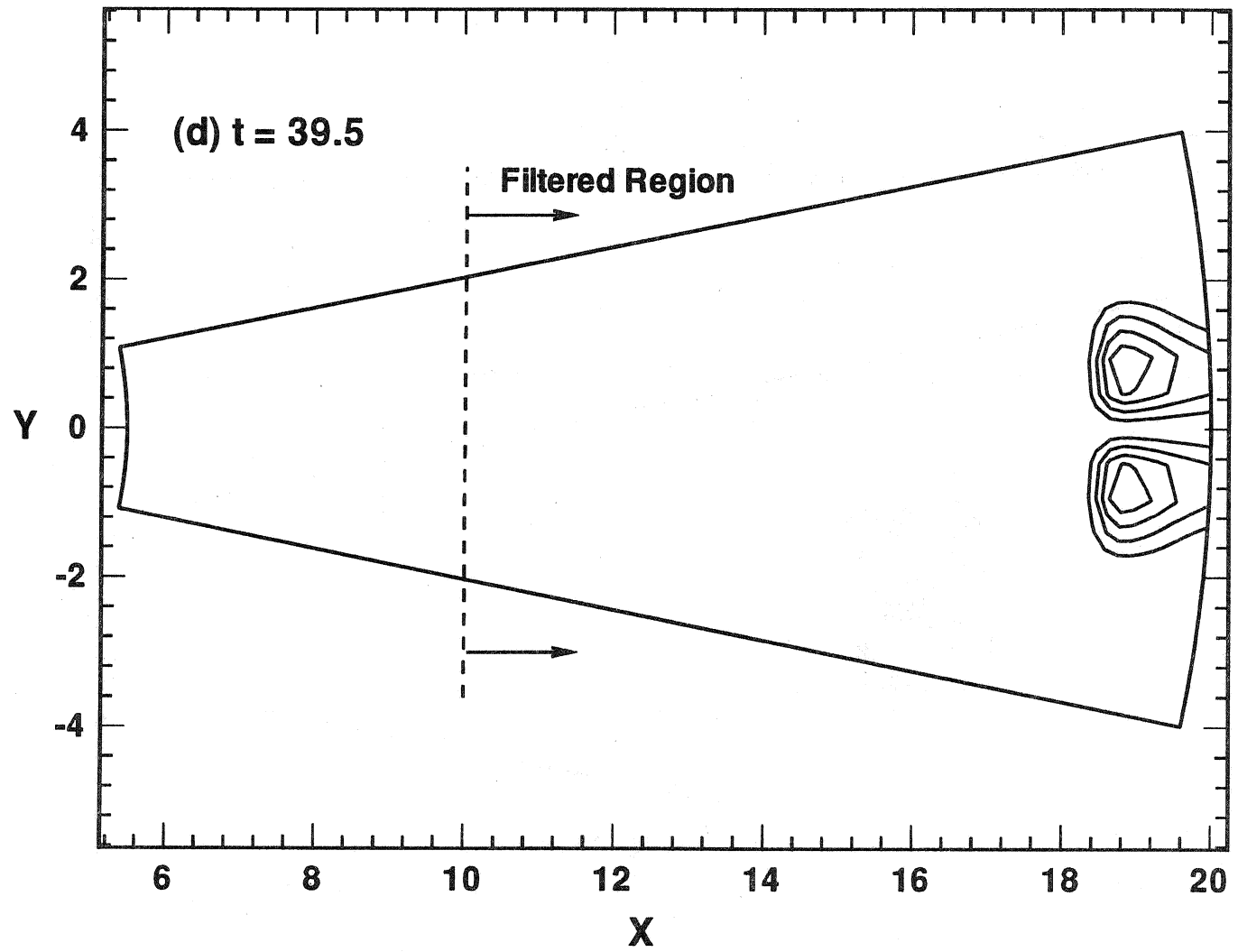

Fig (4d)

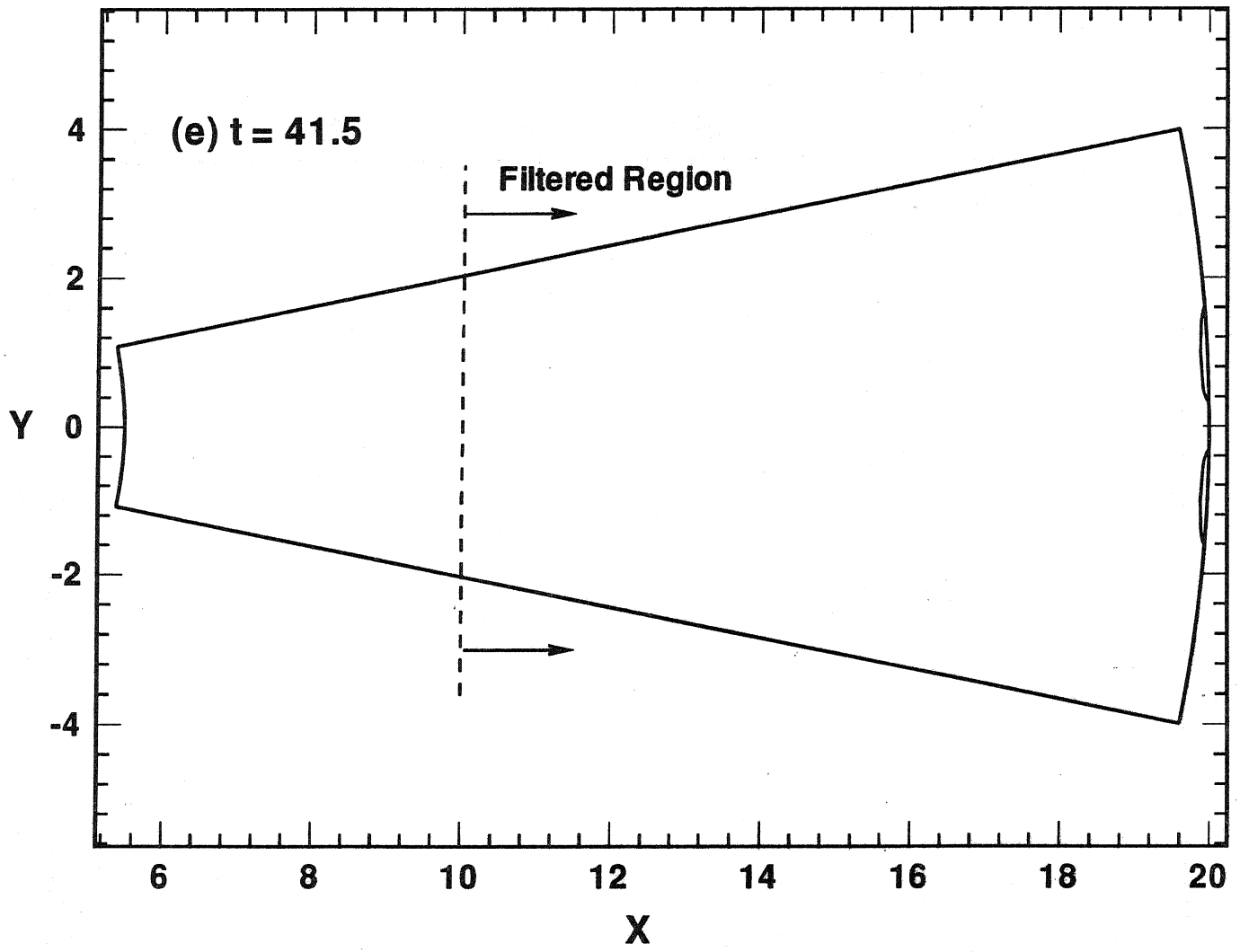

Fig(4e)

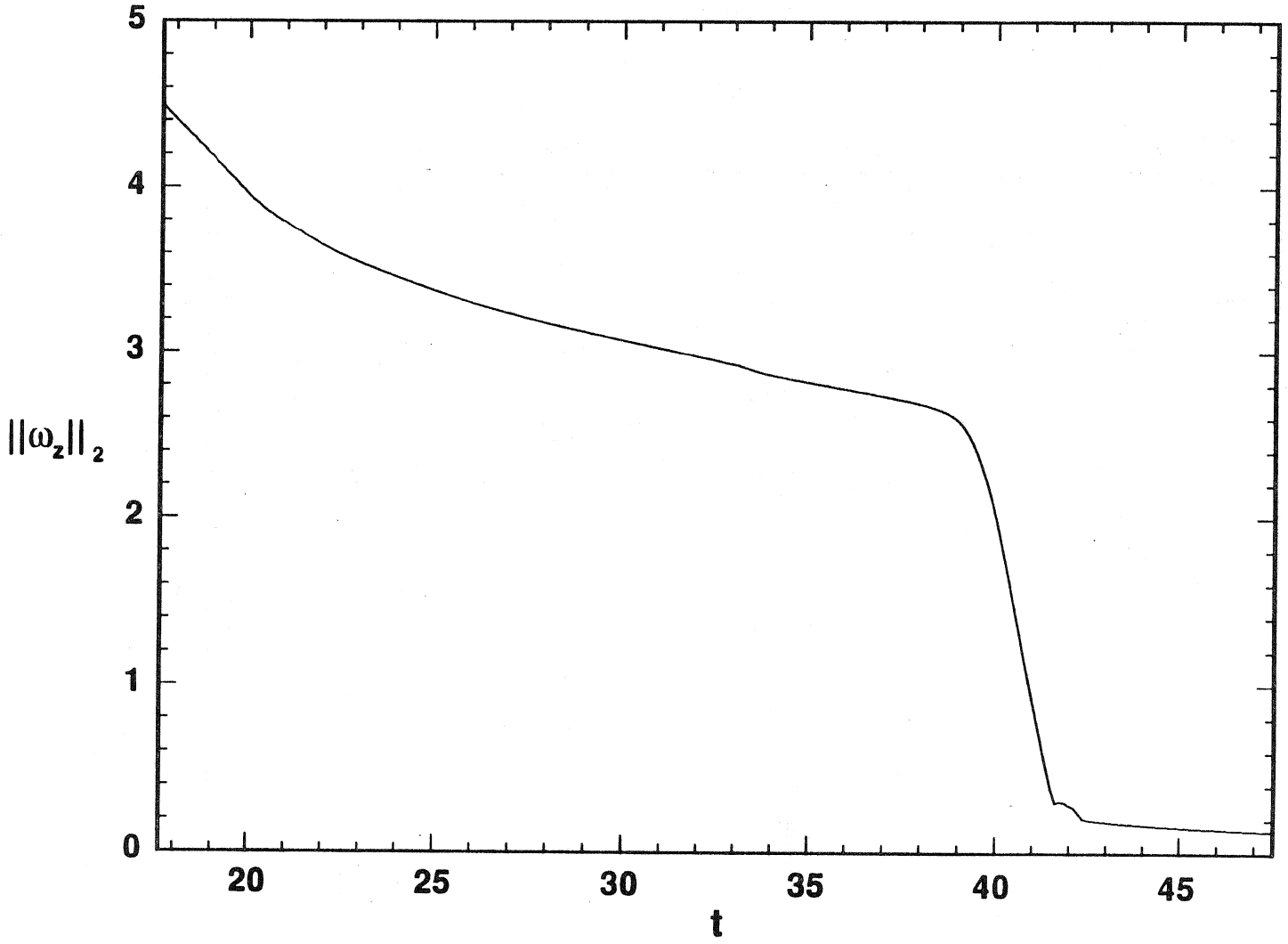

Fig.(5)

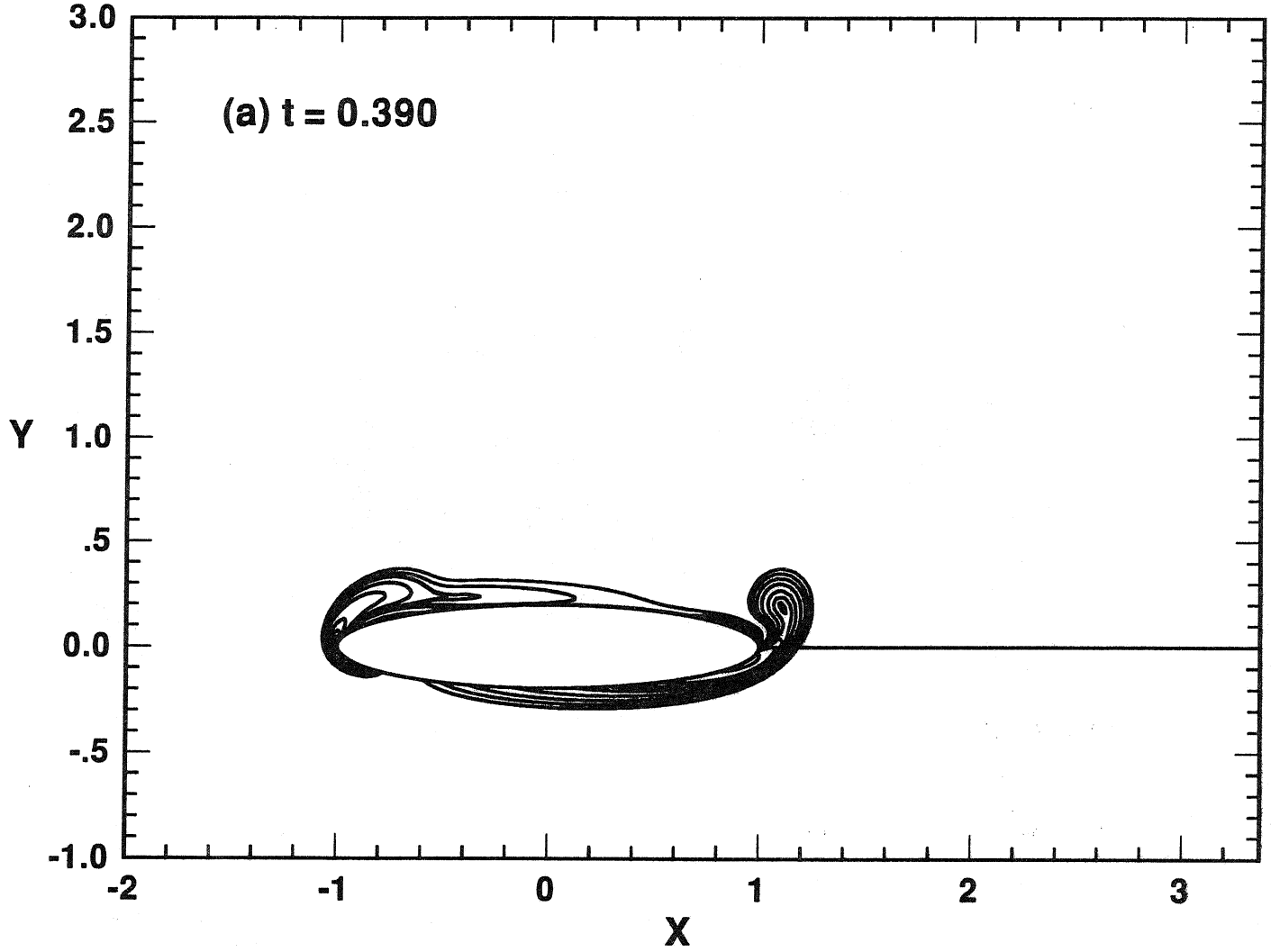

Fig. (6a)

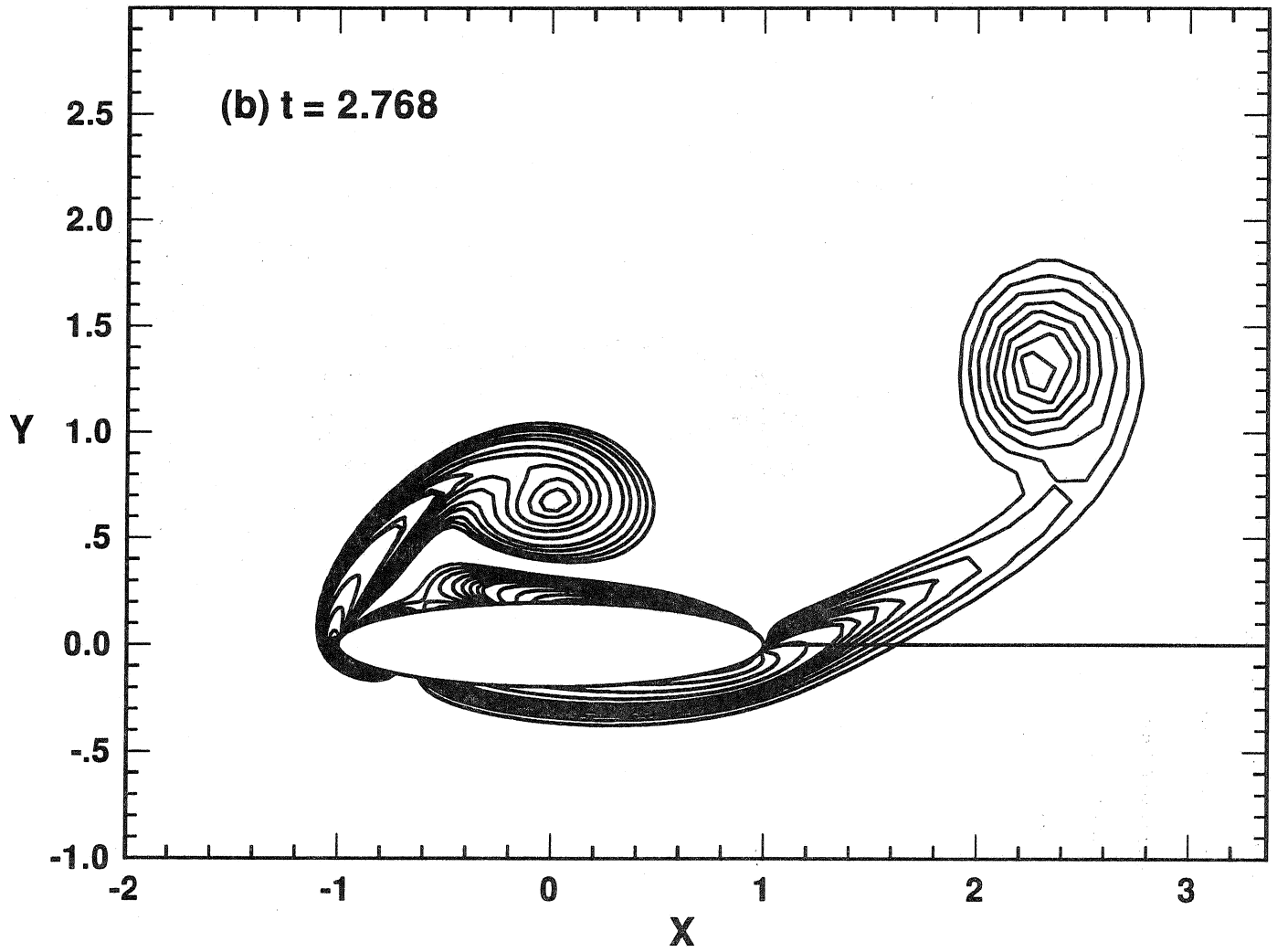

Fig. (6b)

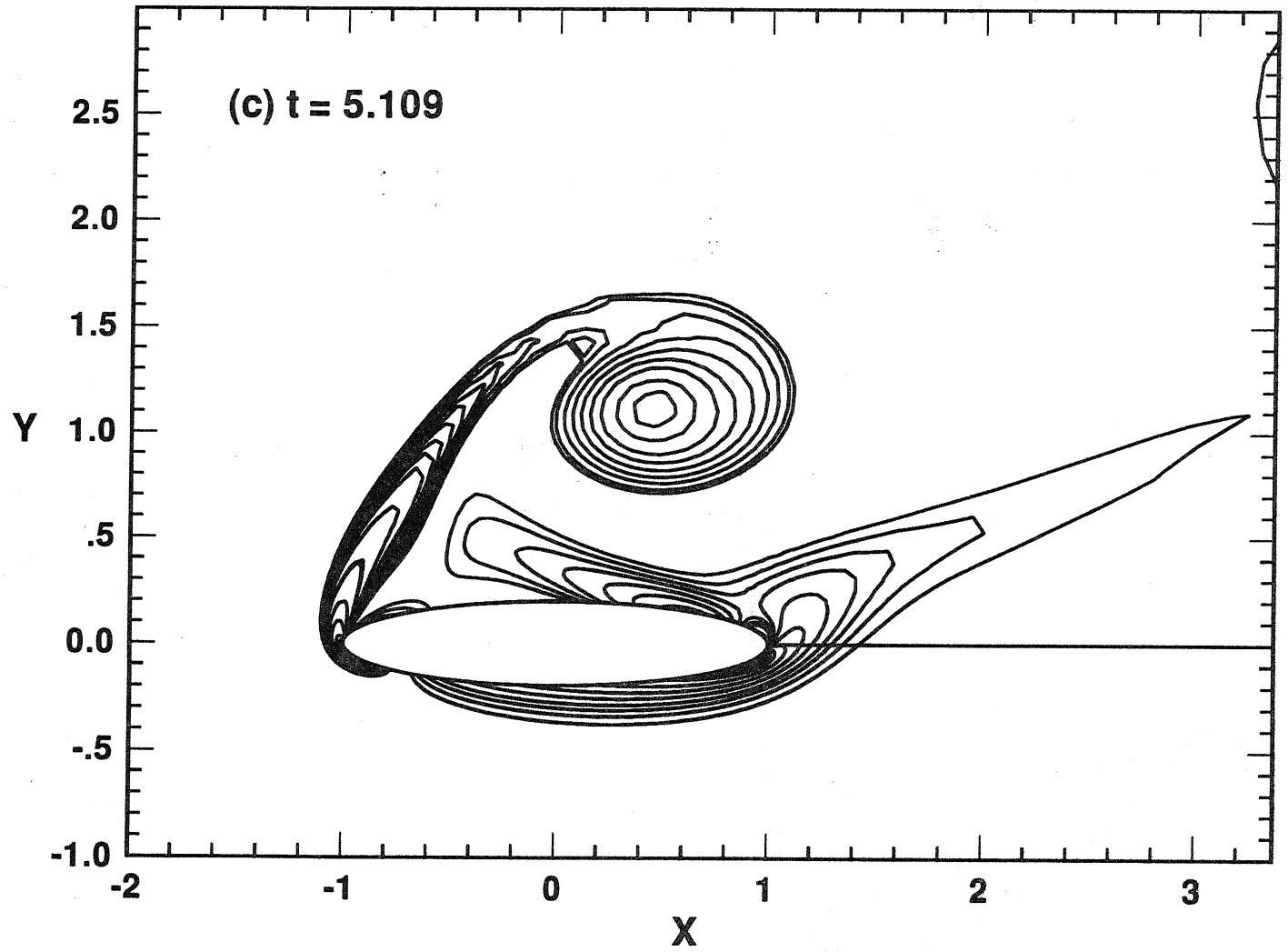

Fig. (6C)

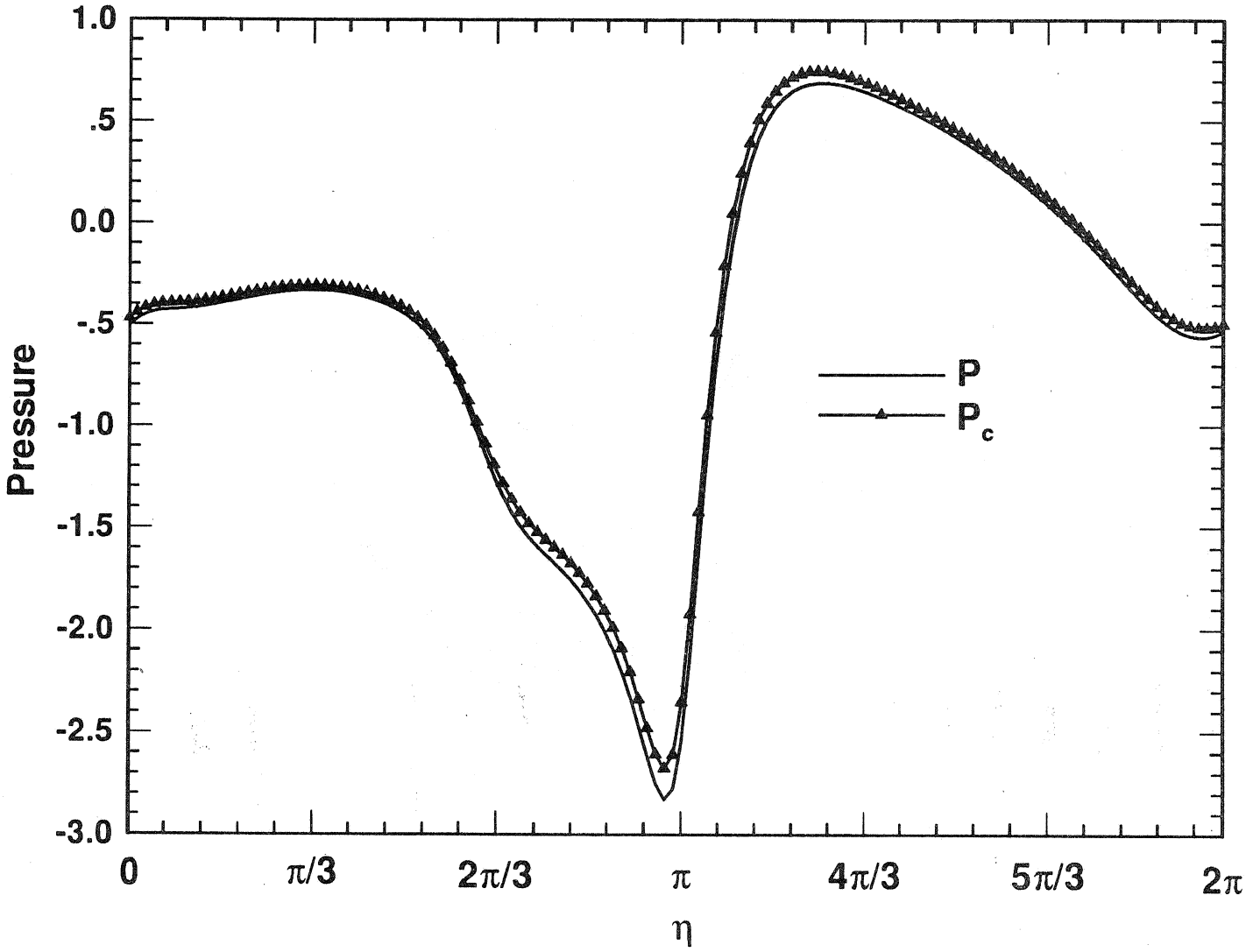

Fig.(7)

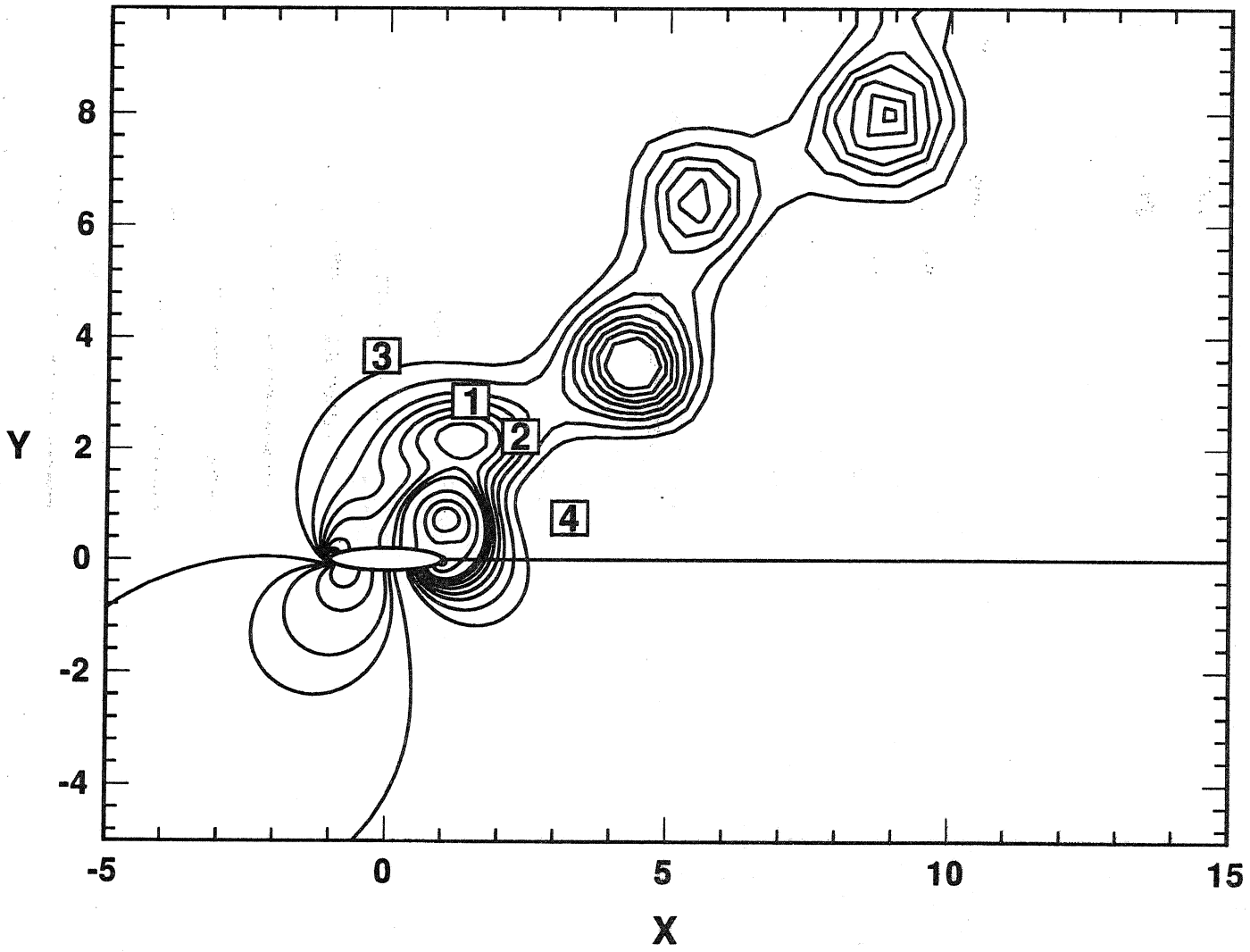

Fig. (8)

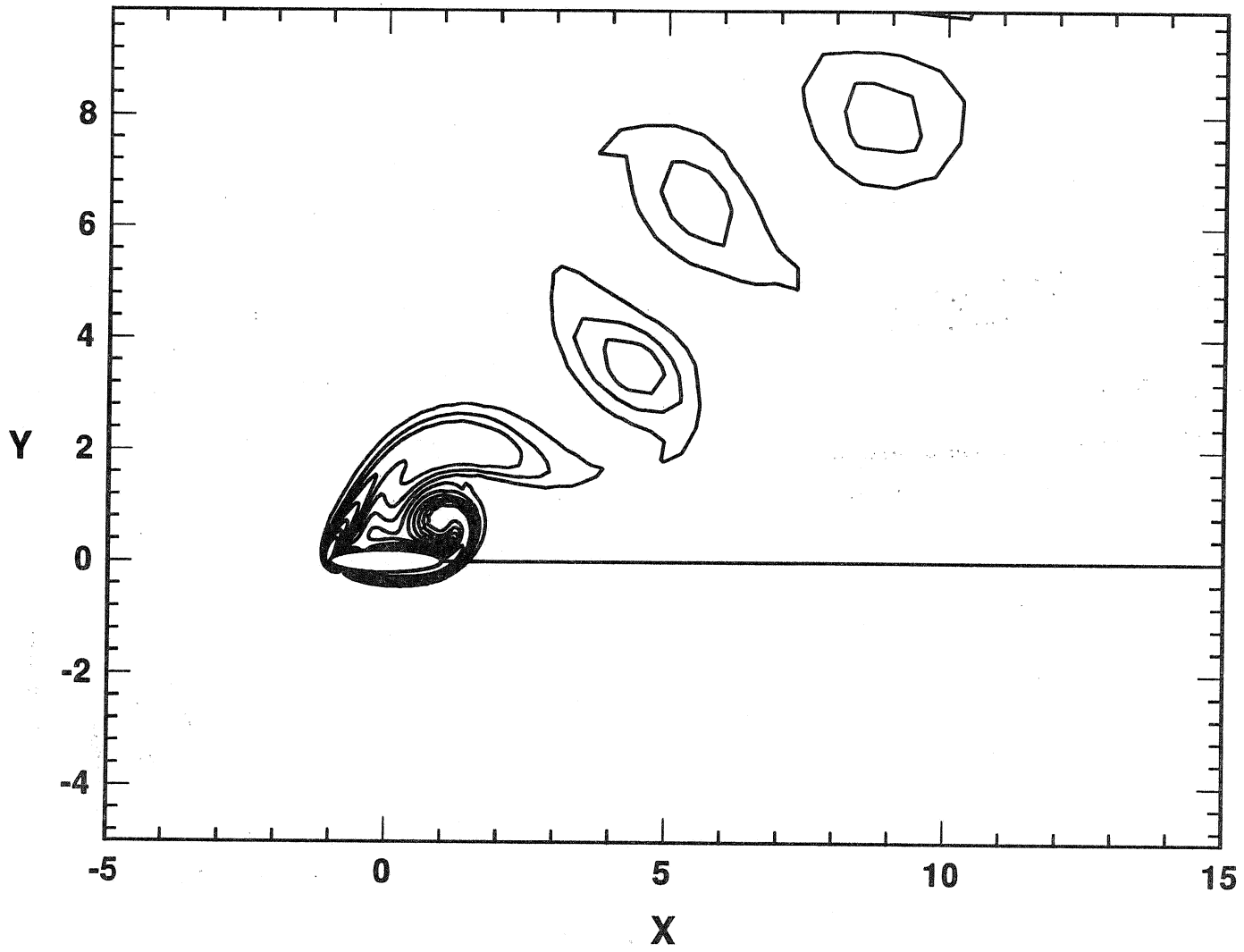

Fig. (9)

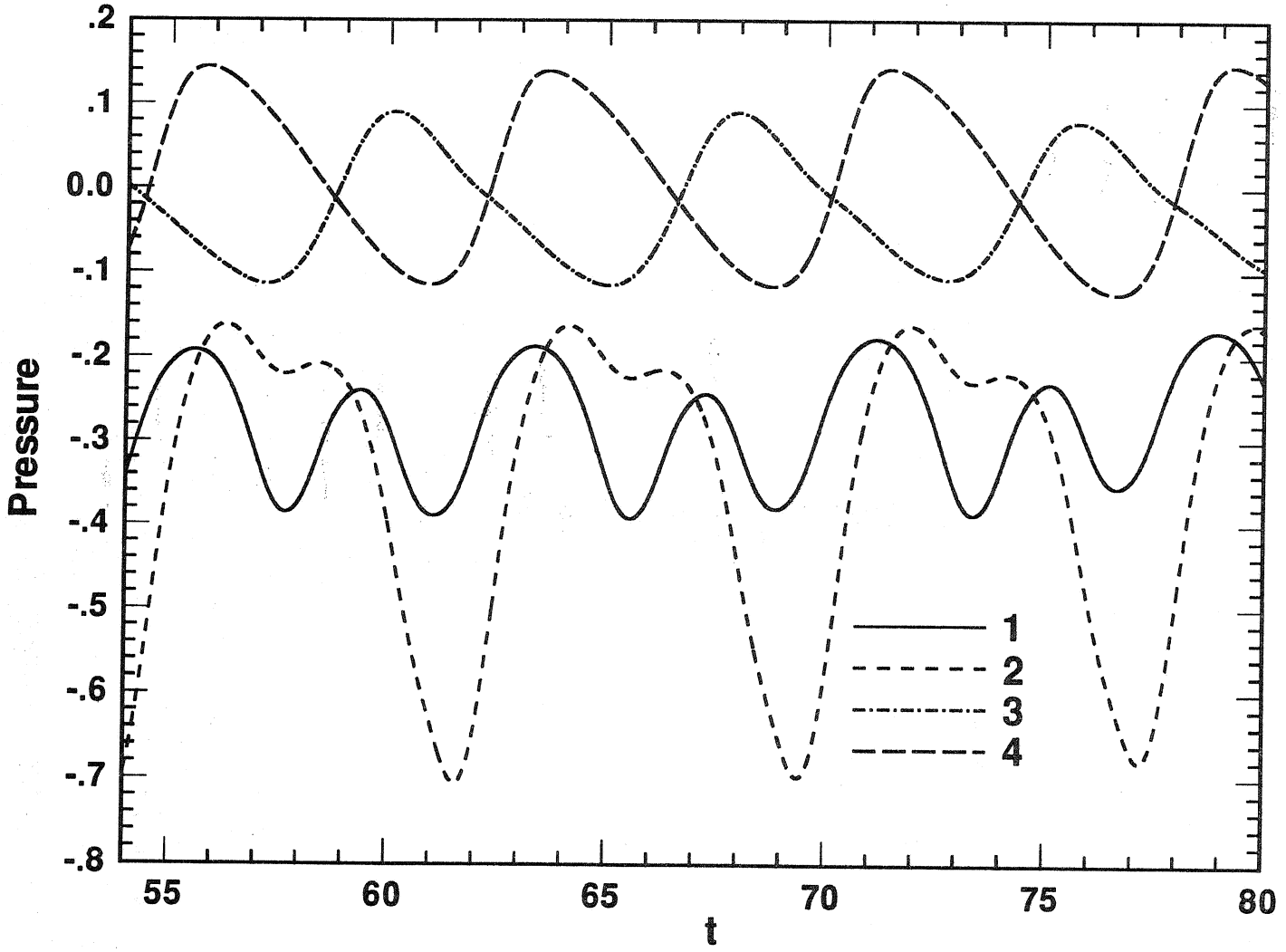

Fig. (10)

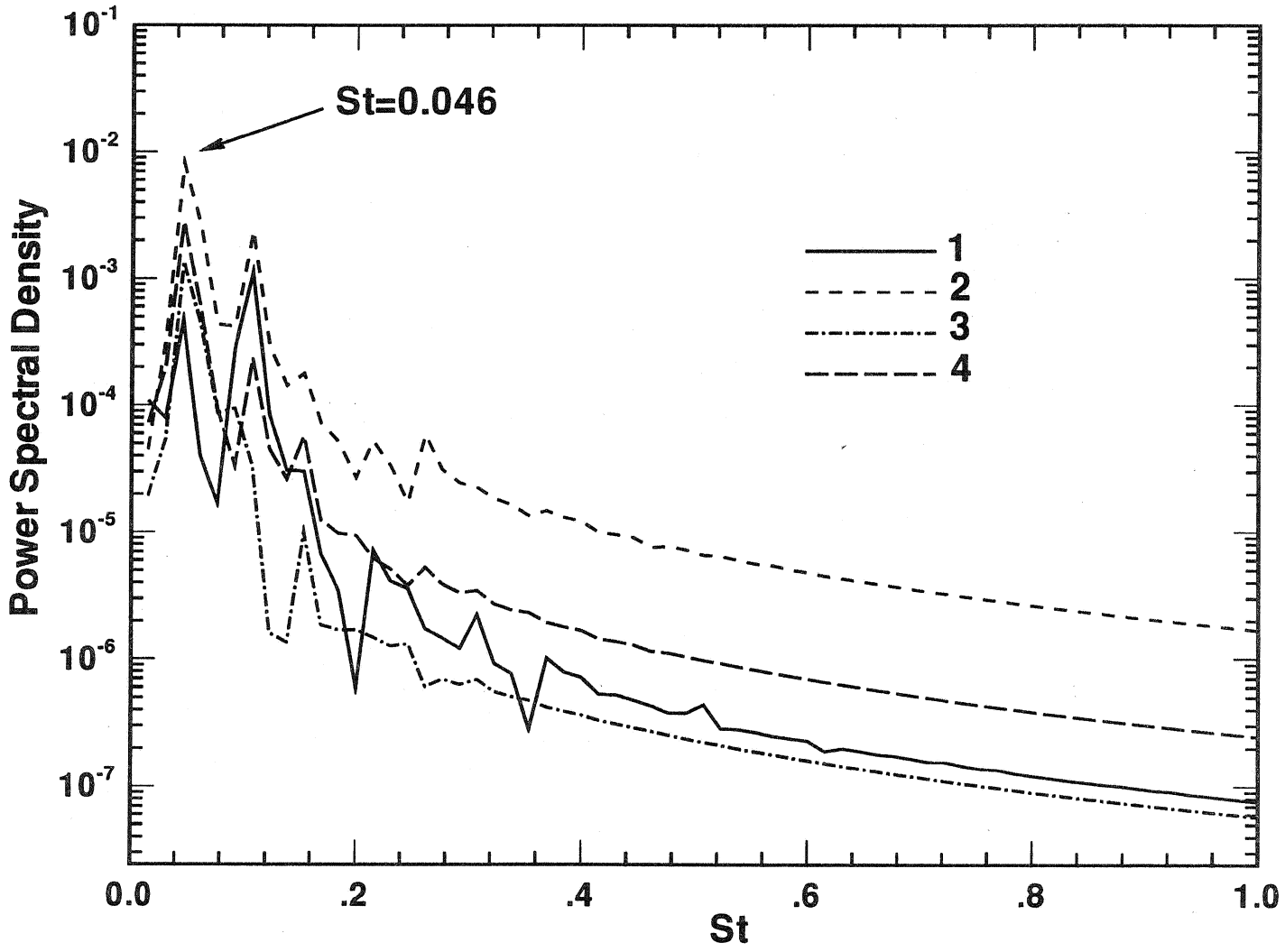
St=0.046
1
2
3
4
Power Spectral Density
St
10^{-1}
10^{-2}
10^{-3}
10^{-4}
10^{-5}
10^{-6}
10^{-7}
0.0
.2
.4
.6
.8
1.0

Fig. (11)

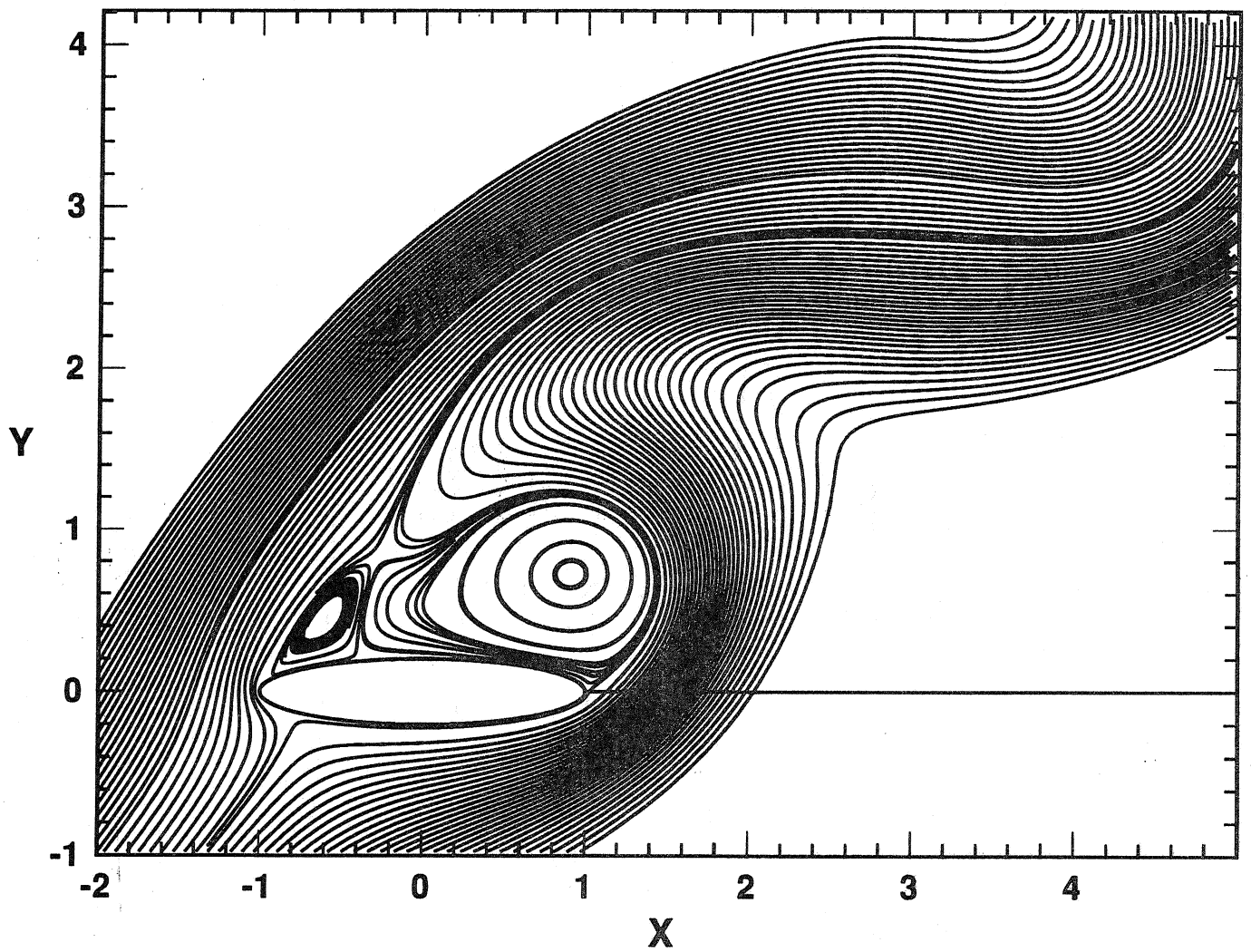

Fig.(12)

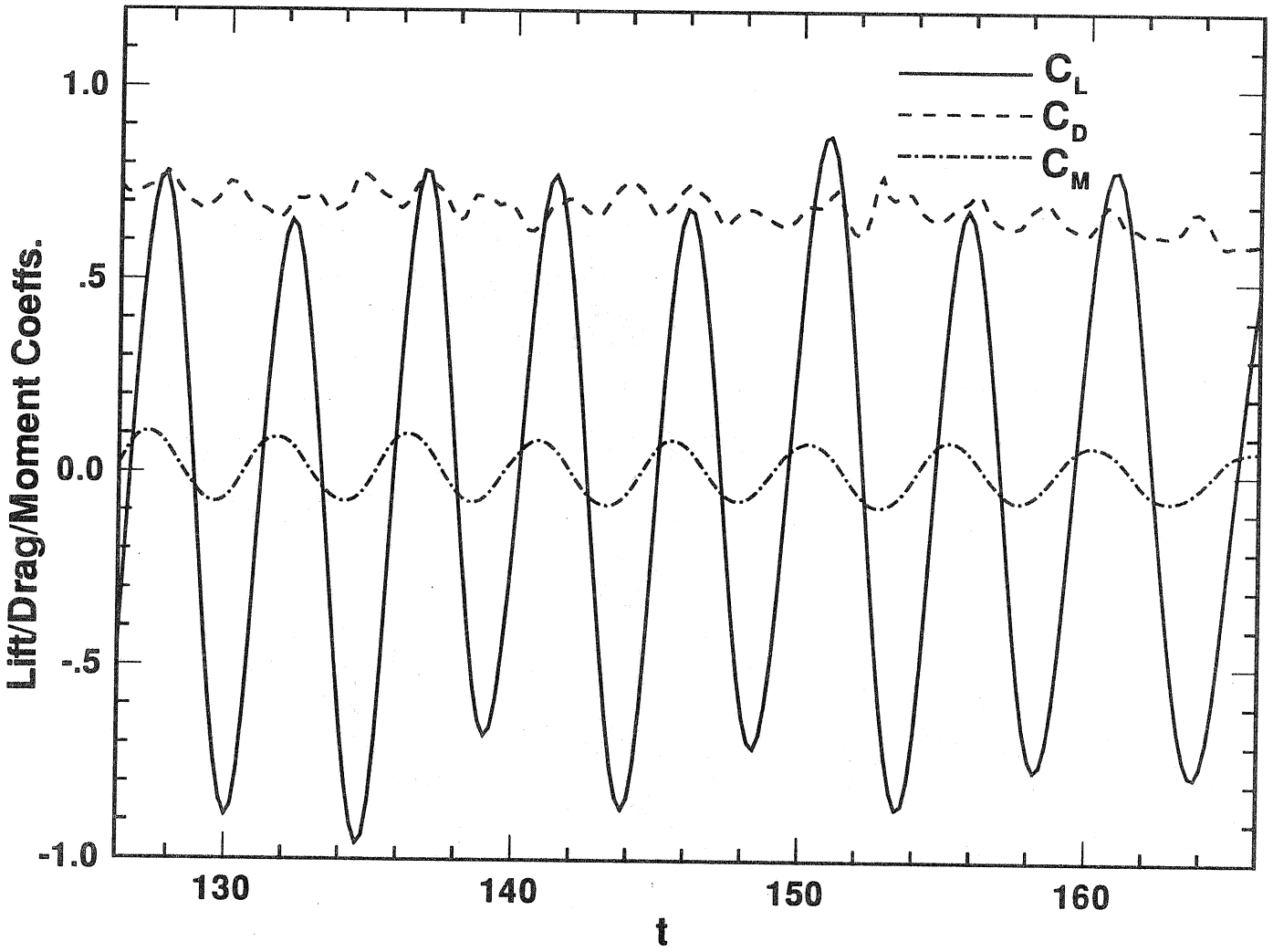

Fig. (13)

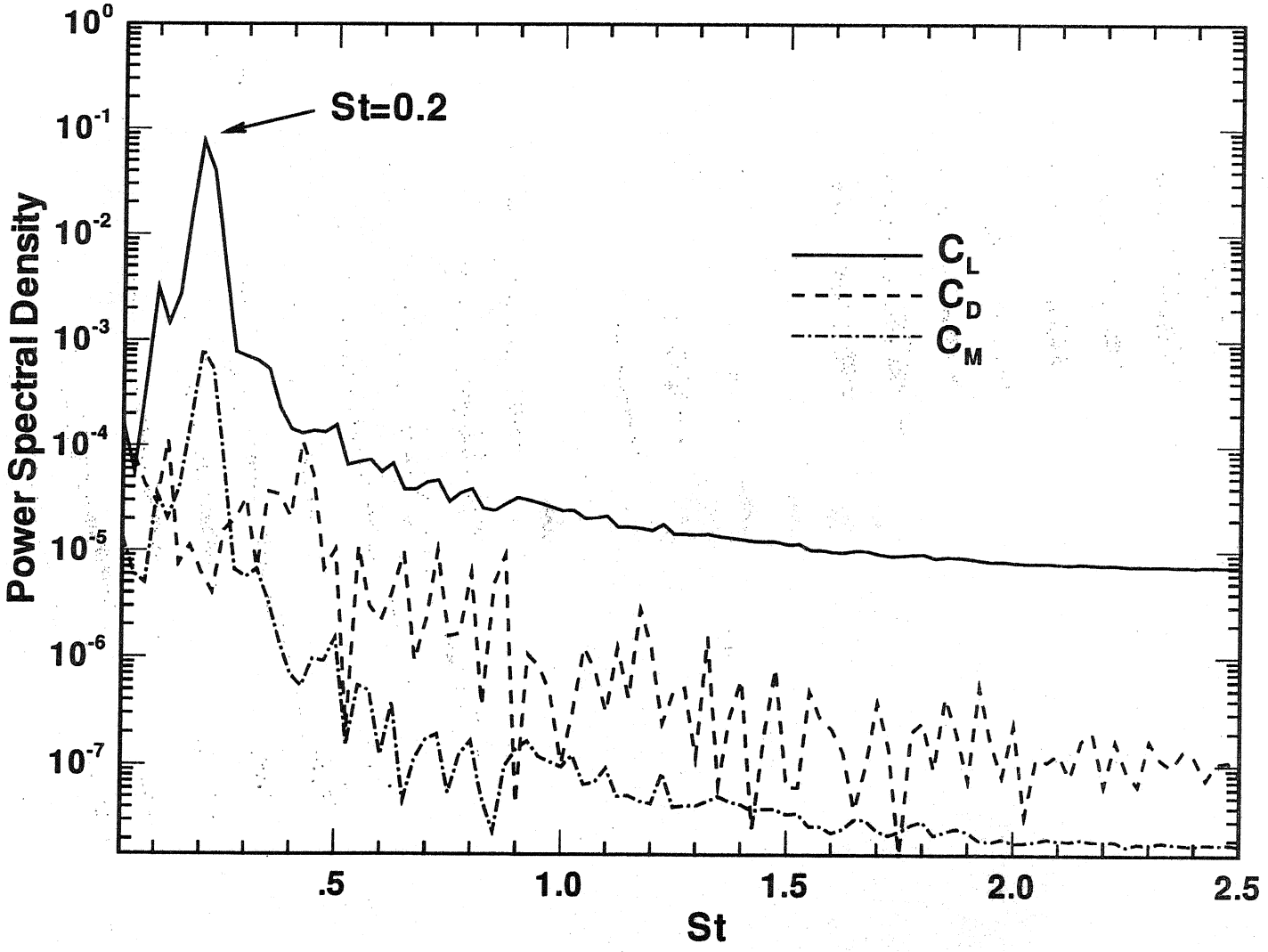
St=0.2
C_L
C_D
C_M
Power Spectral Density
St
10^0
10^{-1}
10^{-2}
10^{-3}
10^{-4}
10^{-5}
10^{-6}
10^{-7}
.5
1.0
1.5
2.0
2.5

Fig. (14)

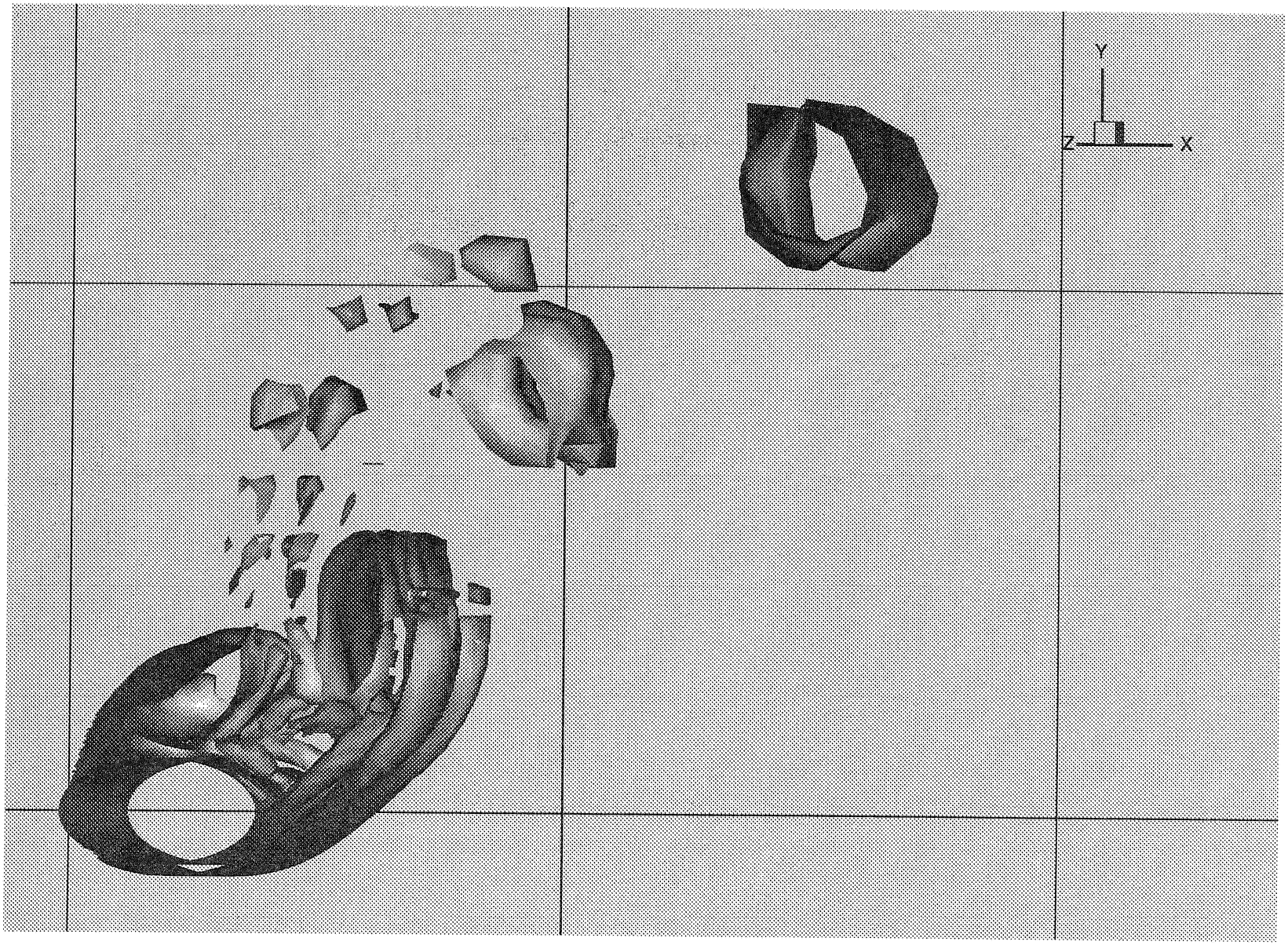

Fig (15)

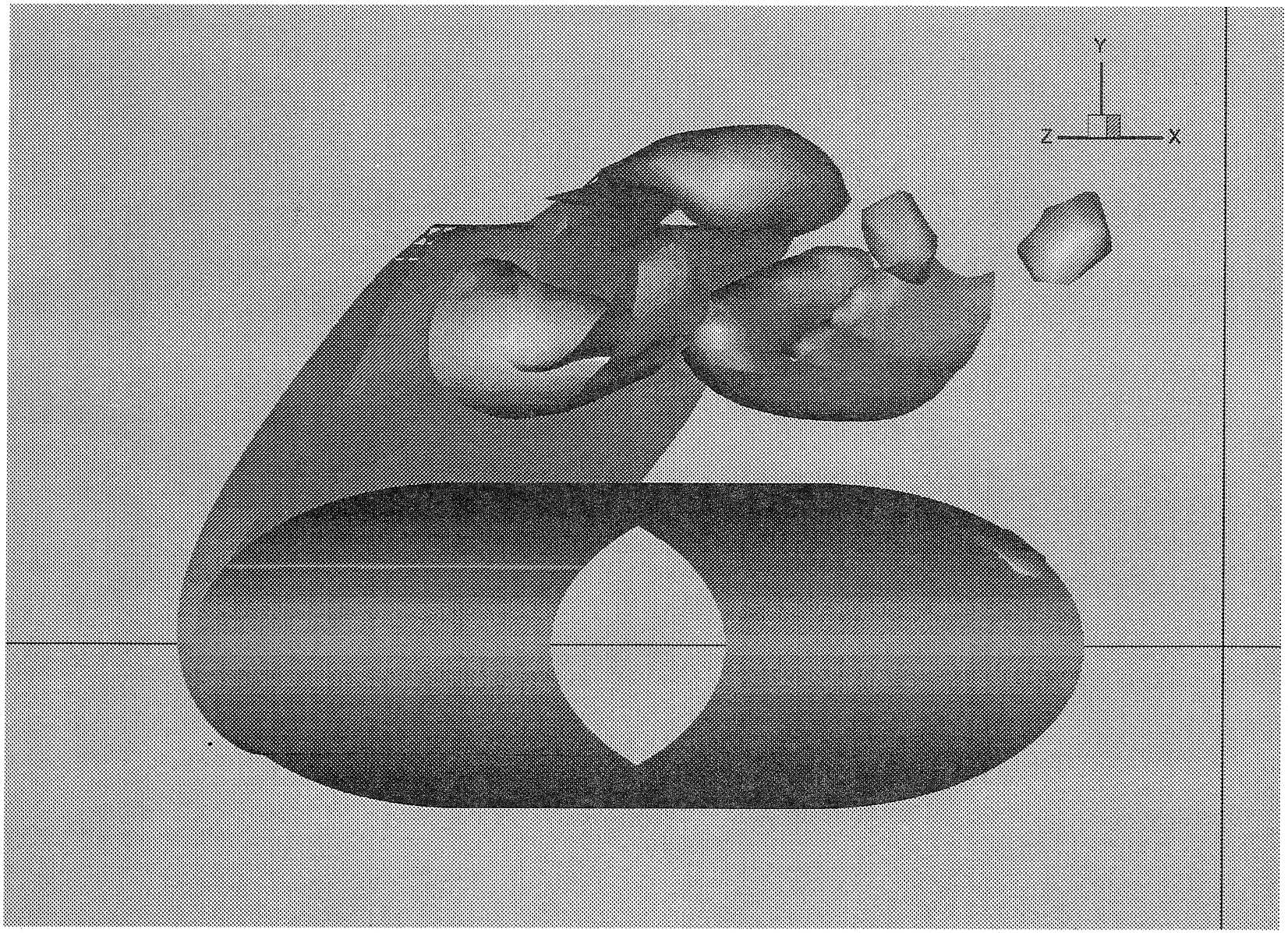

Fig. (16)

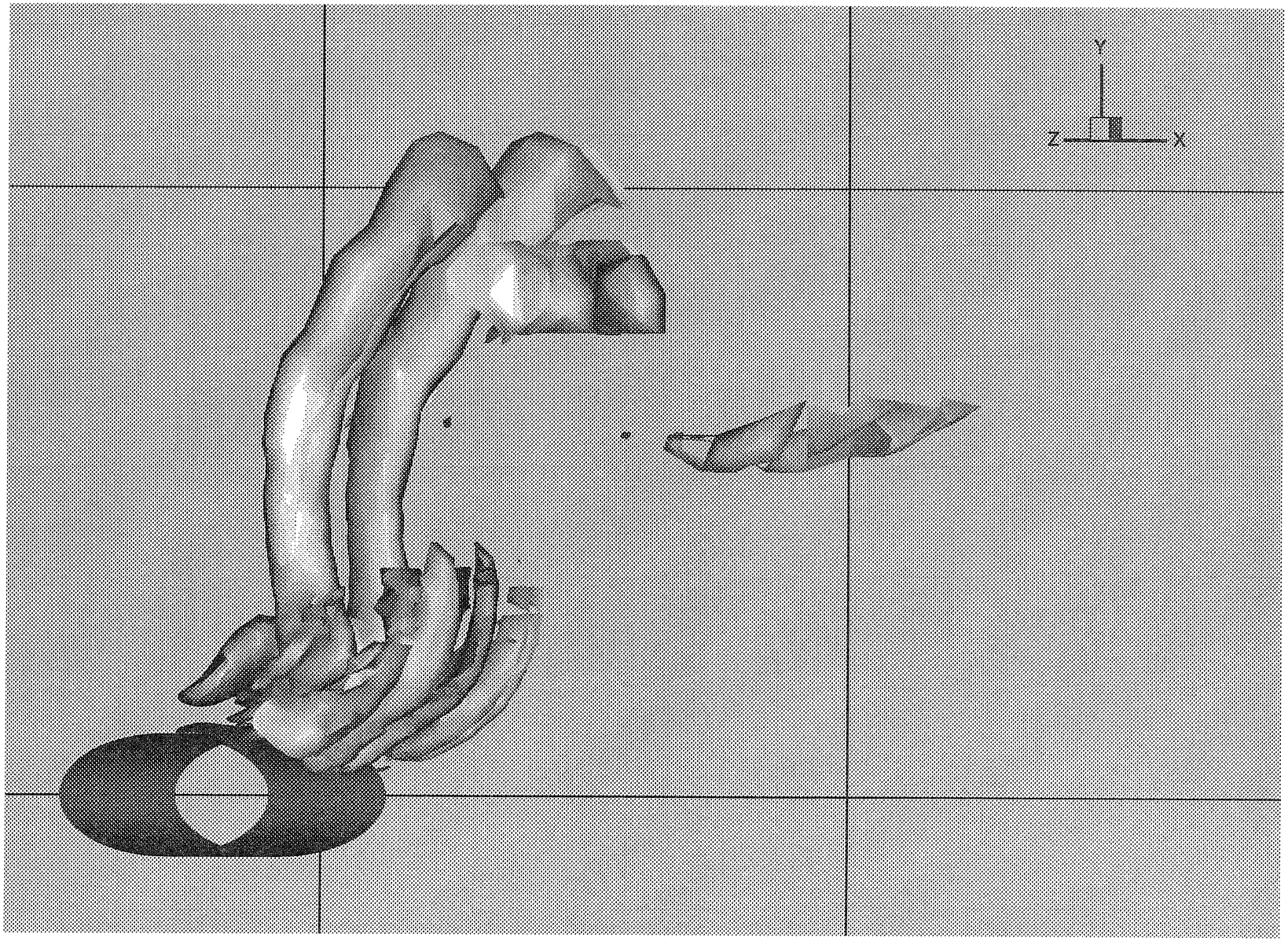

Fig. (17)

List of Recent TAM Reports

No.	*Authors*	*Title*	*Date*
705	Stewart, D. S., and J. B. Bdzil	Asymptotics and multi-scale simulation in a numerical combustion laboratory	Jan. 1993
706	Hsia, K. J., Y.-B. Xin, and L. Lin	Numerical simulation of semi-crystalline nylon 6: Elastic constants of crystalline and amorphous parts	Jan. 1993
707	Hsia, K. J., and J. Q. Huang	Curvature effects on compressive failure strength of long fiber composite laminates	Jan. 1993
708	Jog, C. S., R. B. Haber, and M. P. Bendsøe	Topology design with optimized, self-adaptive materials	Mar. 1993
709	Barkey, M. E., D. F. Socie, and K. J. Hsia	A yield surface approach to the estimation of notch strains for proportional and nonproportional cyclic loading	Apr. 1993
710	Feldsien, T. M., A. D. Friend, G. S. Gehner, T. D. McCoy, K. V. Remmert, D. L. Riedl, P. L. Scheiberle, and J. W. Wu	Thirtieth student symposium on engineering mechanics, J. W. Phillips, coord.	Apr. 1993
711	Weaver, R. L.	Anderson localization in the time domain: Numerical studies of waves in two-dimensional disordered media	Apr. 1993
712	Cherukuri, H. P., and T. G. Shawki	An energy-based localization theory: Part I—Basic framework	Apr. 1993
713	Manring, N. D., and R. E. Johnson	Modeling a variable-displacement pump	June 1993
714	Birnbaum, H. K., and P. Sofronis	Hydrogen-enhanced localized plasticity—A mechanism for hydrogen-related fracture	July 1993
715	Balachandar, S., and M. R. Malik	Inviscid instability of streamwise corner flow	July 1993
716	Sofronis, P.	Linearized hydrogen elasticity	July 1993
717	Nitzsche, V. R., and K. J. Hsia	Modelling of dislocation mobility controlled brittle-to-ductile transition	July 1993
718	Hsia, K. J., and A. S. Argon	Experimental study of the mechanisms of brittle-to-ductile transition of cleavage fracture in silicon single crystals	July 1993
719	Cherukuri, H. P., and T. G. Shawki	An energy-based localization theory: Part II—Effects of the diffusion, inertia and dissipation numbers	Aug. 1993
720	Aref, H., and S. W. Jones	Chaotic motion of a solid through ideal fluid	Aug. 1993
721	Stewart, D. S.	Lectures on detonation physics: Introduction to the theory of detonation shock dynamics	Aug. 1993
722	Lawrence, C. J., and R. Mei	Long-time behavior of the drag on a body in impulsive motion	Sept. 1993
723	Mei, R., J. F. Klausner, and C. J. Lawrence	A note on the history force on a spherical bubble at finite Reynolds number	Sept. 1993
724	Qi, Q., R. E. Johnson, and J. G. Harris	A re-examination of the boundary layer attenuation and acoustic streaming accompanying plane wave propagation in a circular tube	Sept. 1993
725	Turner, J. A., and R. L. Weaver	Radiative transfer of ultrasound	Sept. 1993
726	Yogeswaren, E. K., and J. G. Harris	A model of a confocal ultrasonic inspection system for interfaces	Sept. 1993
727	Yao, J., and D. S. Stewart	On the normal detonation shock velocity–curvature relationship for materials with large activation energy	Sept. 1993
728	Qi, Q.	Attenuated leaky Rayleigh waves	Oct. 1993
729	Sofronis, P., and H. K. Birnbaum	Mechanics of hydrogen–dislocation–impurity interactions: Part I—Increasing shear modulus	Oct. 1993
730	Hsia, K. J., Z. Suo, and W. Yang	Cleavage due to dislocation confinement in layered materials	Oct. 1993
731	Acharya, A., and T. G. Shawki	A second-deformation-gradient theory of plasticity	Oct. 1993
732	Michaleris, P., D. A. Tortorelli, and C. A. Vidal	Tangent operators and design sensitivity formulations for transient nonlinear coupled problems with applications to elasto-plasticity	Nov. 1993
733	Michaleris, P., D. A. Tortorelli, and C. A. Vidal	Analysis and optimization of weakly coupled thermo-elasto-plastic systems with applications to weldment design	Nov. 1993

(continued)

List of Recent TAM Reports (cont'd)

No.	*Authors*	*Title*	*Date*
734	Ford, D. K., and D. S. Stewart	Probabilistic modeling of propellant beds exposed to strong stimulus	Nov. 1993
735	Mei, R., R. J. Adrian, and T. J. Hanratty	Particle dispersion in isotropic turbulence under the influence of non-Stokesian drag and gravitational settling	Nov. 1993
736	Dey, N., D. F. Socie, and K. J. Hsia	Static and cyclic fatigue failure at high temperature in ceramics containing grain boundary viscous phase: Part I—Experiments	Nov. 1993
737	Dey, N., D. F. Socie, and K. J. Hsia	Static and cyclic fatigue failure at high temperature in ceramics containing grain boundary viscous phase: Part II—Modelling	Nov. 1993
738	Turner, J. A., and R. L. Weaver	Radiative transfer and multiple scattering of diffuse ultrasound in polycrystalline media	Nov. 1993
739	Qi, Q., and R. E. Johnson	Resin flows through a porous fiber collection in pultrusion processing	Dec. 1993
740	Weaver, R. L., W. Sachse, and K. Y. Kim	Transient elastic waves in a transversely isotropic plate	Dec. 1993
741	Zhang, Y., and R. L. Weaver	Scattering from a thin random fluid layer	Dec. 1993
742	Weaver, R. L., and W. Sachse	Diffusion of ultrasound in a glass bead slurry	Dec. 1993
743	Sundermeyer, J. N., and R. L. Weaver	On crack identification and characterization in a beam by nonlinear vibration analysis	Dec. 1993
744	Li, L., and N. R. Sottos	Predictions of static displacements in 1–3 piezocomposites	Dec. 1993
745	Jones, S. W.	Chaotic advection and dispersion	Jan. 1994
746	Stewart, D. S., and J. Yao	Critical detonation shock curvature and failure dynamics: Developments in the theory of detonation shock dynamics	Feb. 1994
747	Mei, R., and R. J. Adrian	Effect of Reynolds-number-dependent turbulence structure on the dispersion of fluid and particles	Feb. 1994
748	Liu, Z.-C., R. J. Adrian, and T. J. Hanratty	Reynolds-number similarity of orthogonal decomposition of the outer layer of turbulent wall flow	Feb. 1994
749	Barnhart, D. H., R. J. Adrian, and G. C. Papen	Phase-conjugate holographic system for high-resolution particle image velocimetry	Feb. 1994
750	Qi, Q., W. D. O'Brien Jr., and J. G. Harris	The propagation of ultrasonic waves through a bubbly liquid into tissue: A linear analysis	Mar. 1994
751	Mittal, R., and S. Balachandar	Direct numerical simulation of flow past elliptic cylinders	May 1994